Precocious neuronal differentiation and disrupted oxygen responses in Kabuki syndrome

Giovanni A. Carosso[1,2], Leandros Boukas[1,2,3], Jonathan J. Augustin[2,4,5], Ha Nam Nguyen[6], Briana L. Winer[2], Gabrielle H. Cannon[2], Johanna D. Robertson[2], Li Zhang[2], Kasper D. Hansen[2,3], Loyal A. Goff[2,5], Hans T. Bjornsson*[2,7,8,9]

[1]Predoctoral Training Program in Human Genetics, McKusick-Nathans Institute of Genetic Medicine, Johns Hopkins University School of Medicine, Baltimore, United States.
[2]McKusick-Nathans Institute of Genetic Medicine, Johns Hopkins University School of Medicine, Baltimore, United States.
[3]Department of Biostatistics, Johns Hopkins University School of Medicine, Baltimore, United States.
[4]Predoctoral Training Program in Biochemistry, Cellular, and Molecular Biology, Johns Hopkins University School of Medicine, Baltimore, United States.
[5]Solomon H. Snyder Department of Neuroscience, Johns Hopkins University School of Medicine, Baltimore, United States.
[6]Institute for Cell Engineering, Johns Hopkins University School of Medicine, Baltimore, United States.
[7]Department of Pediatrics, Johns Hopkins University School of Medicine, Baltimore, United States.
[8]Faculty of Medicine, School of Health Sciences, University of Iceland, Reykjavik, Iceland.
[9]Landspitali University Hospital, Reykjavik, Iceland.

*Correspondence:
Hans Tomas Bjornsson, M.D., Ph.D.
Johns Hopkins University School of Medicine
733 N Broadway, MRB 415
Baltimore, MD, 21205
Telephone: 4105020056
Email: hbjorns1@jhmi.edu

Conflict of interest: The authors declare no conflict of interest.

Abstract

Chromatin modifiers act to coordinate gene expression changes critical to neuronal differentiation from neural stem/progenitor cells (NSPCs). Lysine-specific methyltransferase 2D *(KMT2D)* encodes a histone methyltransferase that promotes transcriptional activation, and is frequently mutated in cancers and in the majority (>70%) of patients diagnosed with the congenital, multisystem intellectual disability (ID) disorder Kabuki syndrome 1 (KS1). Critical roles for KMT2D are established in various non-neural tissues, but the effects of KMT2D loss in brain cell development have not been described. We conducted parallel studies of proliferation, differentiation, transcription, and chromatin profiling in KMT2D-deficient human and mouse models to define KMT2D-regulated functions in neurodevelopmental contexts, including adult-born hippocampal NSPCs in vivo and in vitro. We report cell-autonomous defects in proliferation, cell cycle, and survival, accompanied by early NSPC maturation in several KMT2D-deficient model systems. Transcriptional suppression in KMT2D-deficient cells indicated strong perturbation of hypoxia-responsive metabolism pathways. Functional experiments confirmed abnormalities of cellular hypoxia responses in KMT2D-deficient neural cells, and accelerated NSPC maturation in vivo. Together, our findings support a model in which loss of KMT2D function suppresses expression of oxygen-responsive gene programs important to neural progenitor maintenance, resulting in precocious neuronal differentiation in a mouse model of KS1.

Graphical Abstract

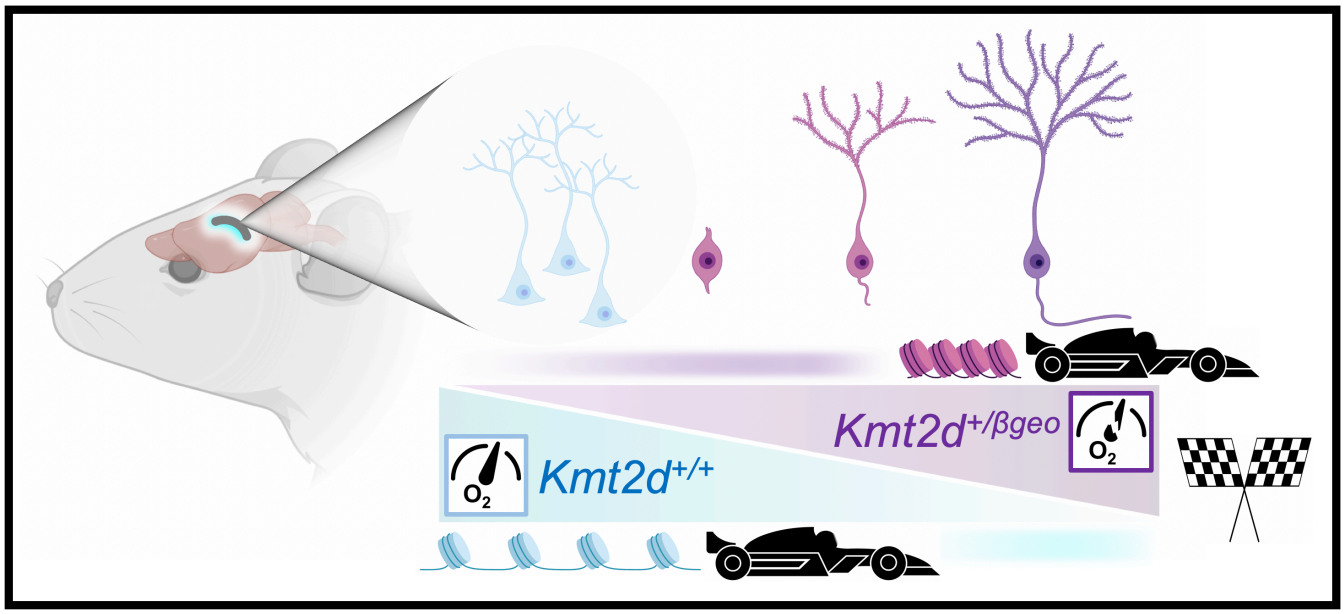

54 **Introduction**

55 Trithorax group proteins promote chromatin accessibility by exerting antagonistic functions
56 against Polycomb group transcriptional suppressors to activate gene expression (1). Fine-tuning of
57 cell type transitions during neuronal development from NSPCs depends critically on this duality, as
58 evidenced by severe neurodevelopmental defects caused by variants in numerous chromatin-
59 modifying genes (2). Loss-of-function variants in genes encoding two such enzymes, KMT2D and
60 lysine-specific demethylase 6A (KDM6A/UTX) cause the ID disorder KS (KS1 and KS2, respectively) (3,
61 4). Up to 74% (5) of KS cases result from mutations in *KMT2D* (KS1), encoding a major histone H3
62 lysine 4 (H3K4) methyltransferase which catalyzes chromatin-opening modifications at context-
63 specific targets. Developmental requirements for KMT2D in cardiac precursors (6), B cells (7, 8),
64 muscle and adipose (9), and epithelial tissues (10) have been linked, respectively, to *KMT2D*-
65 associated cardiac, immunologic, and oncogenic phenotypes (11), yet the effects of KMT2D
66 deficiency in neurodevelopment are not yet understood.

67 We previously described a mouse model of KS1, *Kmt2d*$^{+/\beta geo}$, demonstrating characteristic
68 features including craniofacial abnormalities and visuospatial memory impairments, associated with
69 decreased adult-born hippocampal NSPCs in the dentate gyrus (DG) (12). Decreased DG grey matter
70 volume was subsequently observed in KS1 patients (13). The continual birth and integration of new
71 neurons makes adult neurogenesis the most potent form of lifelong plasticity in the mammalian brain
72 (14), though recent studies have disagreed on its extent in humans (15–17). During late embryonic
73 stages, a subset of multipotent NSPCs persists in the DG (18), becoming subject to an array of
74 intrinsic and extrinsic factors affecting NSPC maintenance, i.e. self-renewal, proliferation, and
75 neuronal differentiation, throughout adult life. Mounting evidence tightly links metabolic rewiring (19)
76 and hypoxic states in the DG (20, 21) to cell-intrinsic regulation of NSPC maintenance.

77 Here, we find that KMT2D deficiency strongly suppresses metabolic gene expression and
78 leads to reduced proliferation, abnormal hypoxia responses, and precocious neuronal maturation in
79 multiple KS1 model systems. Importantly, these phenotypes were validated in vivo in a KS1 mouse
80 model, supporting a role for these abnormalities in the pathogenesis of KS1-associated ID.

Results

Genetic ablation of the *Kmt2d* SET methyltransferase domain disrupts proliferation and cell cycle in a cell-autonomous manner

We first selected the HT22 mouse hippocampal neuronal cell line (22) for analysis of KMT2D catalytic function in neuronal context. gDNA sequence encoding the Su(var)3-9, enhancer-of-zeste and trithorax (SET) methyltransferase domain was deleted by CRISPR-Cas9 with an upstream small guide RNA ($sgRNA^{up}$) in exon 52, and either $sgRNA^{1}$ (exon 54) or $sgRNA^{2}$ (intron 54), resulting in deletions of 565 bp ($Kmt2d^{\Delta 1}$) or 654 bp ($Kmt2d^{\Delta 2}$), respectively, as verified by Sanger DNA sequencing, in silico translation, and PCR (**Supplementary Figure 1A-B**). Targeted cells were clonally expanded to establish heterozygous ($Kmt2d^{+/\Delta}$) and homozygous ($Kmt2d^{\Delta/\Delta}$) cell lines for comparison against the parental wild-type line ($Kmt2d^{+/+}$). Both biological replicate alleles, $Kmt2d^{\Delta 1}$ and $Kmt2d^{\Delta 2}$, were represented in present studies thus the combined data are denoted hereafter simply as $Kmt2d^{+/\Delta}$ or $Kmt2d^{\Delta/\Delta}$. *Kmt2d* mRNA encoded within the targeted region was ~50% decreased in $Kmt2d^{+/\Delta}$ cells and absent in $Kmt2d^{\Delta/\Delta}$ cells, while *Kmt2d* mRNA from exons upstream of the deletion site was unaffected (**Supplementary Figure 1C**). Immunofluorescence against KMT2D, detecting a peptide sequence upstream of deletions (**Supplementary Figure 1D**), demonstrated distinctly nuclear KMT2D distribution in $Kmt2d^{+/+}$ cells but more diffuse distribution in $Kmt2d^{+/\Delta}$ and $Kmt2d^{\Delta/\Delta}$ cells, while we observed uniformly nuclear expression of a neuronal nuclear marker, RNA binding protein fox-1 homolog 3 (RBFOX3), independent of genotype (**Figure 1A**).

Proliferation analysis after equal-density plating revealed cell densities ~52% lower in $Kmt2d^{+/\Delta}$ cells and ~39% lower in $Kmt2d^{\Delta/\Delta}$ cells, compared to wild-type (**Figure 1B**). This defect was supported by dye-based generational tracking, detecting modestly reduced dilution of a fluorescent tracer, i.e. fewer cell divisions, in $Kmt2d^{+/\Delta}$ and $Kmt2d^{\Delta/\Delta}$ daughter cells compared to wild-type (**Figure 1C**, **Supplementary Figure 1E**), while initial dye uptake in parental cells was genotype-independent. Flow cytometric analysis of cell cycle occupancy, using marker of proliferation Ki-67 (KI67) and a DNA label, revealed that $Kmt2d^{+/\Delta}$ cells and $Kmt2d^{\Delta/\Delta}$ cells were enriched for S and G_2 phase, compared to wild-type (**Figure 1D, Supplementary Figure 1F**). To characterize temporal dynamics of cell cycle progression, we synchronized cells in G_2/M phase and analyzed DNA content at timepoints after release (**Figure 1E**). Wild-type cells exited G_2/M phase at higher rates than $Kmt2d^{\Delta/\Delta}$ cells, at 3 hours and up to 18 hours after release. Cell death was profiled by flow cytometric detection of caspase-3/7

112 substrate cleavage to distinguish early apoptotic cells. Compared to wild-types, apoptotic cell
113 proportions were greater in both *Kmt2d*$^{+/\Delta}$ cells (~287%) and *Kmt2d*$^{\Delta/\Delta}$ cells (~478%) (**Figure 1F**).
114 To examine proliferation in primary hippocampal progenitors, we isolated NSPCs from micro-
115 dissected DG of *Kmt2d*$^{+/\beta geo}$ mice and wild-type littermates. NSPCs exhibited characteristic expression
116 of NSPC marker nestin (NES), with a minority of cells expressing mature neuron marker calbindin
117 (CALB) (**Figure 1G**). Cells were plated at equal density and pulsed with cell division marker 5-ethynyl-
118 2′-deoxyuridine (EdU), then quantified by confocal microscopy. Compared to wild-type, *Kmt2d*$^{+/\beta geo}$
119 NSPCs demonstrated lower proliferation rates as measured by EdU incorporation and cell density
120 (**Figure 1H**).
121 Findings of proliferation defects, G_2/M cell cycle delay, and increased apoptosis in
122 hippocampal cells bearing *Kmt2d* inactivation by SET domain deletion, together with proliferation
123 defects in primary *Kmt2d*$^{+/\beta geo}$ hippocampal NSPCs, support a cell-intrinsic role for KMT2D activity in
124 neurodevelopmental contexts.
125
126 **Suppressed transcription of KMT2D-regulated hypoxia response genes upon loss of the KMT2D**
127 **SET methyltransferase domain**
128 We performed high-coverage RNA-seq comparing three *Kmt2d*$^{\Delta/\Delta}$ clones against the parental
129 *Kmt2d*$^{+/+}$ line, each in technical triplicate, followed by differential expression analysis. Libraries
130 clustered robustly by genotype with clear separation of *Kmt2d*$^{\Delta/\Delta}$ cells from *Kmt2d*$^{+/+}$ by Principal
131 Component Analysis (PCA), yielding 575 significant differentially-expressed genes (DEGs) at a False
132 Discovery Rate (FDR) of 0.05 in *Kmt2d*$^{\Delta/\Delta}$ cells compared to *Kmt2d*$^{+/+}$ (**Figure 2A, Supplementary**
133 **Figure 2A-B**, **Supplementary Table 1**). ~76% of DEGs (436 genes) were downregulated in *Kmt2d*$^{\Delta/\Delta}$
134 cells, including known KMT2D targets such as Krueppel-like factor 10 (*Klf10*) (12), revealing strong
135 global transcriptional suppression from *Kmt2d* inactivation. Overrepresentation analysis (ORA)
136 revealed significant enrichment of gene networks among *Kmt2d*$^{\Delta/\Delta}$ down DEGs, including glycolysis
137 and hypoxia-inducible factor 1A (HIF1A) signaling, while *Kmt2d*$^{\Delta/\Delta}$ upregulated DEGs were enriched in
138 fewer networks (**Figure 2B**).
139 We reasoned that among *Kmt2d*$^{\Delta/\Delta}$ DEGs, a subset of genes found to also bind KMT2D itself in
140 wild-type cells would more likely represent direct transcriptional consequences of *Kmt2d* inactivation,
141 whereas non-bound DEGs could reflect secondary effects. We performed chromatin
142 immunoprecipitation followed by high-throughput sequencing (ChIP-seq) using a previously validated
143 ChIP-grade KMT2D antibody (9) in *Kmt2d*$^{+/+}$ HT22 cells. We identified 3,756 KMT2D binding peaks

144 significantly enriched over input (**Supplementary Table 2**), of which ~10% occur inside promoters,
145 ~33% (1,235 peaks) occur within 5 kb of a transcription start site (TSS±5kb), and ~25% occur within 2
146 kb (**Supplementary Figure 2C-F**). To account for promoter and enhancer interactions (9, 10, 23), we
147 reasoned that TSS±5kb peaks, compared to more distal peaks, are more likely to reflect KMT2D cis-
148 regulatory functions on proximal genes, so we refer to these as KMT2D-bound genes. The 1,463
149 observed KMT2D-bound genes (**Supplementary Table 3**) were significantly enriched in mRNA 3'UTR
150 binding, rho GTPase signaling, circadian clock, translation, oxidative stress, HIF1A signaling, and
151 other pathways (**Supplementary Figure 2G**).

152 We then intersected KMT2D-bound genes with *Kmt2d*$^{\Delta/\Delta}$ DEGs to reveal 74 putative direct
153 target genes (**Supplementary Table 3**), of which ~85% (63 genes) were downregulated (**Figure 2C**),
154 including insulin-like growth factor 1 (*Igf1*), and fos-like antigen 2 (*Fosl2*). At least 20 observed KMT2D-
155 bound, *Kmt2d*$^{\Delta/\Delta}$ DEGs were previously described as KMT2D targets in other tissues (7, 24). KMT2D-
156 bound, *Kmt2d*$^{\Delta/\Delta}$ down-DEGs were most significantly enriched for pathways including face
157 morphogenesis, glycolysis, hypoxia response, and proliferation, and surprisingly, 29 of these 63 genes
158 are also HIF1A-regulated (25). Although craniofacial features associate with KS1, enrichment of face
159 morphogenesis genes in HT22 cells likely reflects pleiotropic gene functions. KMT2D ChIP-seq peaks
160 on HIF1A-regulated genes clustered at promoters and enhancers, often overlapping CpG islands in
161 genes such as *Fosl2*, with others clustering at alternative TSSs, as in retinoic acid receptor alpha
162 (*Rara*), or in enhancer-like peaks, as in DNA-damage-inducible transcript 4 (*Ddit4*) (**Figure 2D**,
163 **Supplementary Figure 2H**).

164 A large fraction of KMT2D-bound, *Kmt2d*$^{\Delta/\Delta}$ DEGs control oxygen-responsive metabolism,
165 warranting interrogation of shared KMT2D and HIF1A binding sites. We first intersected KMT2D
166 peaks with HIF1A peaks previously found in embryonic heart (26), finding 423 overlapped regions
167 (**Figure 2E**). Like KMT2D, HIF1A showed ~10% of peaks located inside promoters, but among shared
168 KMT2D/HIF1A-bound peaks this fraction approached ~40%, supporting cooperative regulatory
169 activity (**Supplementary Figure 2I**). We identified 289 TSS±5kb genes, as defined above, for these
170 overlapped KMT2D/HIF1A-bound peaks, including 8 *Kmt2d*$^{\Delta/\Delta}$ DEGs (**Supplementary Table 3**).To
171 check if KMT2D/HIF1A-bound genes generalize to other tissues we next interrogated independent
172 gene sets having experimentally validated, hypoxia-induced HIF1A binding in the promoter (27). Of 86
173 validated genes, 5 were KMT2D-bound, *Kmt2d*$^{\Delta/\Delta}$ down-DEGs, 23.3-fold more than expected by
174 chance (Fisher's Exact Test, p=4.74e-6) (**Supplementary Table 3**). Of 81 genes validated in three or

175 more tissues, 3 were KMT2D-bound, *Kmt2d*$^{\Delta/\Delta}$ down-DEGs: *Klf10*, *Rara*, and *Ddit4* (Fisher's Exact
176 Test, p=0.002).
177 Given the prevalence of oxygen response genes among *Kmt2d*$^{\Delta/\Delta}$ down-DEGs and shared
178 KMT2D/HIF1A targets, we hypothesized a positive regulatory role for KMT2D in transcriptional
179 responses to hypoxia in HT22 cells. We subjected *Kmt2d*$^{+/+}$, *Kmt2d*$^{+/\Delta}$, and *Kmt2d*$^{\Delta/\Delta}$ cells to normoxia
180 (21% O_2) or hypoxia (1% O_2), and measured hypoxia-induced gene expression responses. Analysis of
181 canonical HIF1A targets, vascular endothelial growth factor A (*Vegfa*), Bcl2/adenovirus E1B 19-KD
182 protein-interacting protein 3 (*Bnip3*), DNA-damage-inducible transcript 3 (*Ddit3*), and cyclin-dependent
183 kinase inhibitor 1A (*Cdkn1A*), in *Kmt2d*$^{+/+}$ cells revealed robust upregulations upon hypoxic exposure;
184 in contrast, *Kmt2d*$^{+/\Delta}$ and *Kmt2d*$^{\Delta/\Delta}$ cell lines failed to induce these genes to comparable levels (**Figure
185 2F, Supplementary Figure 2J**). In hypoxic conditions, stabilized HIF1A undergoes nuclear
186 translocation, i.e. activation. We therefore quantified nucleus-localized HIF1A fluorescence under
187 normoxia (21% O_2) and hypoxia (1% O_2) (**Supplementary Figure 2K**). Unexpectedly, in normoxia,
188 *Kmt2d*$^{\Delta/\Delta}$ cells exhibited >2-fold greater HIF1A activation than *Kmt2d*$^{+/+}$ cells. Upon hypoxic exposure,
189 HIF1A activation doubled in wild-type cells, but failed to respond in *Kmt2d*$^{+/\Delta}$ cells and *Kmt2d*$^{\Delta/\Delta}$ cells.
190 Taken together, our data suggest that KMT2D plays an important role in positively regulating
191 HIF1A-inducible, oxygen-responsive metabolic gene programs in neuronal cells.
192
193 **KS1 patient-derived cells recapitulate KMT2D-associated defects in proliferation and cell cycle**
194 We reprogrammed skin biopsy fibroblasts to generate induced pluripotent stem cells (iPSCs)
195 from a previously described female KS1 patient bearing a heterozygous nonsense *KMT2D* mutation
196 (c.7903C>T:p.R2635*) with characteristic facial features, congenital heart disease, and visuospatial
197 memory impairments (28). We selected KS1 iPSCs (KS1-1) bearing normal 46, XX karyotype
198 (**Supplementary Figure 3A**) and characteristic morphology (**Figure 3A**) for comparison against
199 previously described iPSC lines from unrelated healthy controls (C1-2, C3-1) (29). *KMT2D* mRNA
200 quantification in KS1 iPSCs confirmed decreased message compared to controls, as expected due to
201 haploinsufficiency (**Supplementary Figure 3B-C**). Quantification after EdU pulse demonstrated lower
202 proliferation rates (~25%) in KS1 iPSCs compared to controls (**Figure 3B**), accompanied by a shift in
203 cell cycle occupancy (**Figure 3C, Supplementary Figure 3D**) favoring G_2/M phase (24% more cells).
204 We next generated NES-expressing NSPCs through parallel differentiation of KS1 and control
205 iPSCs, using an established small molecule inhibition protocol (30). RT-qPCR confirmed decreased
206 *KMT2D* in KS1 NSPCs (**Supplementary Figure 3E**), and cells displayed normal morphology

207 independent of genotype (**Figure 3D, Supplementary Figure 3F**). EdU incorporation rates revealed
208 KS1 NSPCs had a marked proliferation defect (~47% reduced, **Figure 3E**) and fewer mitotic divisions
209 (**Supplementary Figure 3G**). KS1 NSPCs did not display a cell cycle defect (**Figure 3F,**
210 **Supplementary Figure 3H**), suggesting either cell-type dependence or loss of this phenotype during
211 in vitro differentiation. Flow cytometry indicated higher proportions of dying cells in KS1 samples
212 compared to controls among both iPSCs (~130%) and NSPCs (~115%) (**Figure 3G, Supplementary**
213 **Figure 3I-J**).
214 To determine whether G_2/M bias, seen in KS1 iPSCs, occurred in unmanipulated primary cells
215 from additional KS1 patients, we analyzed fibroblasts from three molecularly confirmed KS1 patients
216 (KS1-1, KS1-2, KS1-3) and healthy controls. Fibroblasts were synchronized in G_2/M phase followed by
217 flow cytometric analysis of DNA content. At 3 hours post-release, control cells had exited G_2/M phase,
218 in contrast to KS1 cells which remained in G_2/M (**Figure 3H**). Thus, delayed G_2/M exit was consistent
219 in primary, non-reprogrammed cells from three KS1 patients.
220
221 **Transcriptional suppression of metabolic genes in cycling cells, and precocious neuronal**
222 **differentiation in KS1 patient-derived NSPCs**
223 To interrogate transcriptional consequences of *KMT2D* loss in the context of neuronal
224 differentiation, we performed single-cell RNA sequencing (scRNA-seq) in iPSCs and NSPCs from the
225 KS1 patient and controls (**Supplementary Figure 4A**). By inspecting expression of cell-type markers,
226 we confirmed that libraries segregated into clusters reflecting distinct cell identities of the expected
227 lineages (**Supplementary Figure 4B-D**).
228 First, differential expression analysis in iPSCs and NSPCs identified genes downregulated or
229 upregulated in KS1 patient relative to healthy controls (**Supplementary Figure 4E**). KS1 iPSCs
230 displayed strong transcriptional suppression among 421 DEGs, with 372 genes down and 49 genes
231 up (**Supplementary Table 4**). NSPCs showed less directional bias, having 346 significant DEGs
232 among which 147 genes were down and 199 genes were up (**Supplementary Table 5**). Intersection of
233 KS1 iPSC and NSPC DEG lists showed that 40 genes were shared down and 10 genes were shared
234 up (**Supplementary Figure 4F-G, Supplementary Table 6**). Shared down genes included glycolysis
235 genes, aldehyde dehydrogenase 7 family member A1 (*ALDH7A1*), enolase 1 (*ENO1*), and
236 triosephosphate isomerase 1 (*TPI1*), as well as factors important to stem cell maintenance including
237 proliferation-associated protein 2G4 (*PA2G4*) and protein lin-28 homolog A (*LIN28A*). As in *Kmt2d*$^{\Delta/\Delta}$
238 HT22 cells, downregulated genes in KS1 patient iPSCs and NSPCs were significantly enriched for

239 HIF1A direct targets, genes containing the hypoxia-responsive element (HRE) 5'-RCGTG-3' motif, and
240 known hypoxia response genes (**Supplementary Figure 4H**).

241 We next focused on NSPCs from KS1 and controls to interrogate transcriptional effects during
242 neuronal differentiation. We used Uniform Manifold Approximation and Projection (UMAP) to visualize
243 single cells in a manner that displays high-dimensionality data while preserving both local and global
244 relationships (31). Control NSPCs were tightly clustered, indicating similar expression profiles, in
245 contrast to a distinct separation of KS1 cells which gradually lessens in a subset (top) of cells that
246 more closely resemble controls (**Figure 4A**). We then partitioned single-cell libraries into
247 developmentally informative subsets as follows. First, we verified that differences in cell cycle phase
248 composition do not account for KS1-associated differential gene expression in NSPCs
249 (**Supplementary Figure 5A, Supplementary Table 7**). Next, we partitioned cells by stage-specific
250 marker expression to define a differentiation trajectory consisting of early or "cycling" NSPCs,
251 "transitioning" NSPCs, and "differentiating" NSPCs (**Figure 4B**). Cycling cells comprised the majority
252 of NSPCs analyzed and exhibited the greatest KS1-associated expression differences, while
253 expression profiles of transitioning and differentiating NSPCs show gradual convergence of gene
254 expression. We analyzed DEGs exclusively within cycling, transitioning, and differentiating NSPC
255 subsets to determine if particular gene networks drive transcriptional differences in a stage-specific
256 manner (**Figure 4C, Supplementary Table 7**). KS1 DEGs in transitioning NSPCs, and to a lesser
257 extent cycling NSPCs, showed enrichment of genes comprising the Notch signaling pathway including
258 delta-like protein 3 (*DLL3*), protein jagged-1 (*JAG1*), transcription factor HES-5 (*HES5*), and cyclin D1
259 (*CCND1*). Cycling NSPCs had DEGs enriched in glycolysis pathways.

260 Apart from increased rates of KS1 cell death (**Figure 3G**), another possible factor in the
261 observed decrease of proliferative KS1 NSPCs (**Figure 3E**) could be a change in cellular
262 differentiation, such as precocious cell maturation, resulting in depletion of cycling precursors. To
263 explore this by scRNA-seq, we examined markers ranging from immature cells (*PAX6*$^{+}$) to the most
264 differentiated cells (*MAP2*$^{+}$) (**Figure 4D-E**). We further restricted analysis to the transitioning and
265 differentiating, i.e. "maturing" NSPC subset (**Supplementary Figure 5B**), defining a trajectory that
266 enabled parsing of cells into binned deciles of increasing maturation (**Supplementary Figure 5C-H**).
267 Quantification of cell densities revealed strong bias of KS1 NSPCs in the most matured bins relative to
268 controls (**Figure 4F**), i.e. greater representation of mature NSPCs from KS1 than controls. These
269 transcriptional signatures were corroborated experimentally at protein level, finding KS1 NSPCs had

270 increased MAP2 fluorescence and decreased PAX6 fluorescence relative to control using flow
271 cytometry (**Figure 4G-H**).
272 Together, these results link transcriptional suppression of metabolic gene pathways to cell-
273 autonomous proliferation defects in *KMT2D*-deficient KS1 patient-derived stem cell models, and
274 scRNA-seq data suggest that precocious differentiation could contribute to KS1-associated
275 neurodevelopmental defects.
276
277 **In vivo defects of neurogenesis and NSPC differentiation in a *Kmt2d*$^{+/\beta geo}$ mouse model of KS1**
278 Finally, we asked whether proliferative defects, transcriptional suppression, and precocious
279 differentiation phenotypes validate in vivo, using an established KS1 mouse model. *Kmt2d*$^{+/\beta geo}$ mice,
280 bearing a *Kmt2d* truncating mutation, were previously found to exhibit visuospatial memory
281 impairments and fewer doublecortin (DCX^{+}) NSPCs in the DG subgranular zone (SGZ) (12, 32), but
282 NSPC lineage progression in *Kmt2d*$^{+/\beta geo}$ mice has not been characterized.
283 We conducted cell cycle and RNA-seq analysis in *Kmt2d*$^{+/\beta geo}$ mice, using an EdU pulse
284 paradigm to label adult-born cells. We sampled micro-dissected DG within 1 cell cycle (16 hours) to
285 capture the full complement of dividing NSPCs (**Figure 5A**), then purified EdU^{+} nuclei by fluorescence-
286 activated cell sorting (FACS) (**Figure 5B**, **Supplementary Figure 6A**). DNA content analysis revealed
287 enrichment of G_2/M phase in *Kmt2d*$^{+/\beta geo}$ EdU^{+} DG nuclei (**Figure 5C**). We next profiled transcription by
288 RNA-seq in purified EdU^{+} DG nuclei, yielding 827 DEGs (**Supplementary Figure 6B-C**,
289 **Supplementary Table 8**). The 416 down-regulated genes in *Kmt2d*$^{+/\beta geo}$ nuclei were enriched for
290 misfolded protein binding, TCA cycle, proteasome complex, oxygen response, and poly(A) RNA-
291 binding genes. Given the observed downregulation of poly(A) RNA-binding genes, we considered the
292 possibility that improper 3'UTR-mediated mRNA metabolism could lead to accumulation of transcripts
293 influencing NSPC maturation. Indeed, despite little overall bias toward up or downregulation in
294 *Kmt2d*$^{+/\beta geo}$ DG nuclei, interrogating positive regulators of neuronal differentiation revealed a marked
295 predominance of pro-neural transcripts upregulated, having only 3 genes down but 14 genes up,
296 including copine-1 (*Cpne1*), focal adhesion kinase 1 (*Ptk2*), ras-related protein RAB11A (*Rab11A*), and
297 retinoblastoma-associated protein 1 (*Rb1*). Interestingly, KS1 patient NSPCs also showed upregulated
298 pro-neural genes such as nuclear receptor subfamily 2, group F, member 1 (*NR2F1*) and pro-neural
299 transcription factor HES-1 (*HES1*), while *Kmt2d*$^{\Delta/\Delta}$ HT22 cells had upregulated brain-derived
300 neurotrophic factor (*Bdnf*) and neuron-specific microtubule component (*Tubb3*/*Tuj1*). Such pro-neural
301 gene expression observed across KS1 models raises the possibility that NSPC differentiation rates
302 could be altered in *Kmt2d*$^{+/\beta geo}$ mice.

303 To examine NSPC lineage progression in vivo, we analyzed stage-specific cell abundances
304 both at steady-state and after birth-dating of adult-born NSPCs by EdU pulse, comparing *Kmt2d*$^{+/\beta geo}$
305 mice to sex- and age-matched *Kmt2d*$^{+/+}$ littermates (**Figure 5D, Supplementary Figure 6D**).
306 At steady-state, we observed significantly fewer NSPCs in *Kmt2d*$^{+/\beta geo}$ mice compared to
307 *Kmt2d*$^{+/+}$ mice at all stages (**Figure 5E**). The cell division marker, minichromosome maintenance
308 complex component 2 (MCM2), distinguished NES^{+} NSPCs in the quiescent (MCM2^{-}) or activated
309 (MCM2^{+}) state. Importantly, quiescent radial glia-like (qRGL, NES^{+}MCM2^{-}) NSPCs were ~39% less
310 numerous in *Kmt2d*$^{+/\beta geo}$ mice, indicating a baseline paucity in the stem cell pool. Activated RGL
311 (aRGL, NES^{+}MCM2^{+}) NSPCs were ~43% less numerous, and intermediate progenitor cell (IPC, NES^{-}
312 MCM2^{+}) NSPCs were ~26% fewer. We confirmed prior observations (12, 32) of fewer neuroblast (NB,
313 DCX^{+}) NSPCs, finding a 28% decrease in *Kmt2d*$^{+/\beta geo}$ mice. By stratifying analysis along the
314 septotemporal axis of the DG, we observed that aRGL NSPC reductions in *Kmt2d*$^{+/\beta geo}$ mice were
315 more pronounced in the septal DG than the temporal region (**Supplementary Figure 6E**), congruous
316 with spatial memory defects (12) localized to the septal DG (33). Because DCX^{+} NSPCs migrate
317 radially during maturation, we compared radial distances of DCX^{+} cell bodies from the SGZ plane and
318 observed increased distances in *Kmt2d*$^{+/\beta geo}$ mice (**Supplementary Figure 6F**). Finally, despite
319 diminished NSPC populations in *Kmt2d*$^{+/\beta geo}$ mice, we observed no numeric differences among mature
320 neurons (RBFOX3^{+}) (**Supplementary Figure 6G**), nor were gross anatomical differences seen by MRI
321 volumetric analysis (**Supplementary Figure 6H, Supplementary Table 9**).
322 From these data, we then calculated a lineage progression index to approximate the expansion
323 potential of each successive neurogenic cell type. Although *Kmt2d*$^{+/\beta geo}$ mice showed fewer total
324 NSPCs of each type at steady-state, the lineage progression index at each cell-type transition did not
325 differ significantly (**Supplementary Figure 6I**), suggesting that particular cell-type transition
326 impairments are not responsible for the adult neurogenesis defect. However, we did note substantially
327 higher variance of RGL activation rates in *Kmt2d*$^{+/\beta geo}$ mice, suggesting impaired coordination of NSPC
328 mitotic entry (**Supplementary Figure 6J**).
329 Pulse-labeling with marker-based imaging enables precise measurement of birth dates, i.e.
330 mitotic division, of specific cell types. To resolve temporal dynamics of NSPC differentiation in
331 *Kmt2d*$^{+/\beta geo}$ and wild-type mice, we pulsed adult mice with EdU for a period of 2 weeks, during which a
332 subset of labeled DG cells is expected to reach a late NSPC (NB) stage, characterized by radial
333 extension of a DCX^{+} neuronal process. In contrast, another subset of pulsed cells, bearing a NES^{+}
334 qRGL-like process, represents NSPCs that remain in a stem-like state. Thus, by quantifying EdU-
335 labeled cells exhibiting either a DCX^{+} neuronal process (EdU^{+}DCX^{+}) or a NES^{+} qRGL-like process

336 (EdU$^+$NES$^+$) (**Figure 5F, Supplementary Figure 7A**), one can compare relative differentiation status,
337 where a higher proportion of EdU$^+$DCX$^+$ cells would indicate early or precocious maturation. Indeed,
338 though steady-state cell numbers again confirmed fewer total NES$^+$ and DCX$^+$ NSPCs in *Kmt2d*$^{+/\beta geo}$
339 mice compared to wild-types, among pulsed cells the *Kmt2d*$^{+/\beta geo}$ mice exhibited a significantly greater
340 fraction of EdU$^+$DCX$^+$ immature neurons (**Figure 5F**). In other words, *Kmt2d*$^{+/\beta geo}$ DG NSPCs born
341 within the preceding 2 weeks had achieved a more advanced differentiation state than wild-type cells
342 born in the same window.
343 Together, studies of adult neurogenesis dynamics in *Kmt2d*$^{+/\beta geo}$ mice suggest that in vivo
344 neurodevelopmental effects of KMT2D loss recapitulate many phenotypes observed initially in vitro
345 using mouse HT22 cells and KS1 human-derived cells. While comparison of gene expression profiles
346 across these KS1 models revealed few individual genes with shared dysregulation among all models,
347 at network level we observed high enrichment of HIF1A regulatory and RNA metabolism pathways in a
348 comparison of all DEGs in these KS1 models (**Supplementary Figure 8A-D**).
349
350 **Precocious differentiation and reduced hypoxia responses in *Kmt2d*$^{+/\beta geo}$ primary hippocampal**
351 **NSPCs**
352 Cellular oxygen availability has previously been directly linked to maintenance and
353 differentiation of embryonic (33) and adult DG (19) NSPCs. Primary hippocampal NSPCs of *Kmt2d*$^{+/\beta geo}$
354 mice showed increased HIF1A activation compared to wild-type NSPCs, and both genotypes showed
355 increased HIF1A activation upon treatment by HIF1A-stabilizing agent dimethyloxaloylglycine (DMOG)
356 for 12 hours (**Supplementary Figure 9A**). We then subjected NSPCs to a standard in vitro neuronal
357 differentiation protocol, quantifying cell marker expression between 0-8 days (**Supplementary Figure**
358 **10A-B**). Prior to differentiation (day 0), wild-type NSPCs expressed low levels of a mature DG neuron
359 marker, prospero-related homeobox 1 (PROX1), while *Kmt2d*$^{+/\beta geo}$ NSPCs surprisingly showed an
360 increase (**Supplementary Figure 10C**). By measuring expression of a pro-neural transcription factor,
361 achaete-scute homolog 1 (ASCL1), we observed a baseline decrease (day 0) in *Kmt2d*$^{+/\beta geo}$ NSPCs
362 compared to wild-type (**Supplementary Figure 10D**). In contrast, after 2 days in differentiation
363 conditions, *Kmt2d*$^{+/\beta geo}$ NSPCs responded with greater ASCL1 expression compared to wild-types, an
364 effect sustained at 4 and 8 days. DMOG treatment increased ASCL1 levels in both genotypes, though
365 to greater magnitude in wild-type than *Kmt2d*$^{+/\beta geo}$ NSPCs. Together, these data are consistent with a
366 link between cellular hypoxia response and neuronal differentiation in hippocampal NSPCs (20).
367

368 **Discussion**

369 The ID disorder KS1 is caused by mutations in the histone methyltransferase *KMT2D*, but
370 mechanistic links to neurodevelopmental and cognitive consequences in patients are not yet clear.
371 KS1 diagnoses are typically made after childbirth, but the inherent reversibility of chromatin
372 modifications raises the possibility that a detailed understanding of KMT2D activity in neuronal cells
373 could identify molecular targets for postnatal interventions in KS1-associated ID.

374 Here, we report that KMT2D-deficient human and mouse neurodevelopment models, in vitro
375 and in vivo, demonstrate similar patterns of transcriptional suppression, proliferative defects, and
376 precocious cellular differentiation. These phenotypes were cell-autonomous in vitro, suggesting that 1)
377 chromatin and gene expression studies in neurogenic cell types could yield disease-relevant KMT2D
378 targets and 2) these cellular models provide platforms for screening of novel therapeutic strategies or
379 targeted manipulations. We performed transcriptomic and KMT2D profiling in these models and
380 observed systematic suppression of hypoxia response pathways, particularly among HIF1A-regulated
381 genes that are also directly KMT2D-bound in neuronal cells. Physically overlapping KMT2D- and
382 HIF1A-bound genomic loci were observed across tissues, ~40% of these at promoters, raising the
383 possibility of shared etiologies in embryonically distinct KS1-affected organ systems. Furthermore,
384 KMT2D-deficient neuronal cells, in contrast to isogenic wild-type cells, were unable to mount
385 characteristic hypoxia-inducible gene activation responses when exposed to low-oxygen conditions,
386 demonstrating oxygen response defects in KS1 models.

387 The implication of hypoxia response defects in KS1 suggests clinical relevance of recent
388 findings in neurodevelopmental regulation. First, the adult hippocampal NSPC niche harbors locally
389 hypoxic, but dynamic, microenvironments and the hypoxic state positively influences NSPC survival
390 (20, 21). Thus, compromised hypoxia responses could render cells particularly vulnerable to changes
391 in oxygen levels as experienced by maturing NSPCs as they migrate from DG SGZ vasculature.
392 Second, NSPC maturation is coupled to a metabolic rewiring from glycolysis in early NSPCs, to
393 oxidative phosphorylation in maturing neurons. Zheng and colleagues (19) recently found this
394 metabolic switch, marked by suppression of glycolytic genes, to be essential for neuronal maturation.
395 In KS1 neural models we observed suppression of hypoxia-responsive glycolytic genes accompanied
396 by upregulation of pro-neuronal differentiation genes, and demonstrated precocious maturation of DG
397 NSPCs by in vivo pulsing of adult *Kmt2d*$^{+/\beta geo}$ mice, as well as in vitro differentiation of *Kmt2d*$^{+/\beta geo}$
398 primary DG NSPCs. Future studies could determine whether targeted chromatin opening at hypoxia
399 response loci normalizes differentiation dynamics in KS1 NSPCs.

400 Analogous findings regarding premature activation of terminal differentiation genes, reduced
401 proliferation, and precocious maturation in KMT2D-depleted keratinocytes were recently linked to
402 disorganized epidermal stratification (10). Furthermore, in KMT2D-deficient cardiomyocytes, loss of
403 H3K4me2 at KMT2D-bound hypoxia response genes associated with cell cycle and proliferative
404 defects in heart development (6). In contrast, KMT2D deletion in B cells conferred proliferative
405 advantage and impaired cell maturation, despite significant up-regulation of differentiation genes (8,
406 9). Thus, while KMT2D's role in enhancer-mediated gene expression during differentiation is well-
407 established (11), phenotypic manifestations appear cell type- and stage-dependent. We now extend
408 KMT2D-associated phenotypes of transcriptional perturbance, hypoxia response, cell cycle,
409 proliferation, and premature differentiation to neuronal contexts. Phenotypic concordance across
410 tissues of disparate embryonic origin suggests that KMT2D targets important to KS1 phenotypes
411 support basic cellular homeostatic functions related to housekeeping, energy production, and cell
412 cycle progression, rather than genes with purely brain-specific function. Furthermore, we report
413 concordant phenotypes both from nonsense *KMT2D* mutations (patient iPSCs and NSPCs), and
414 mutations limited to the KMT2D SET domain (HT22 cells, *Kmt2d*$^{+/\beta geo}$ mice), indicating that loss of
415 either gene dosage or catalytic function of KMT2D can be pathogenic.

416 Present results indicate that adult hippocampal neurogenesis defects, which we previously
417 found to associate with visuospatial memory defects in *Kmt2d*$^{+/\beta geo}$ mice, are observable at all stages
418 examined, including fewer quiescent NSPCs in the DG which could indicate either post-natal depletion
419 or altered niche development in the embryo. Despite having fewer total NSPCs, by pulse-chase
420 experiments we observed the *Kmt2d*$^{+/\beta geo}$ NSPC population to achieve a more advanced maturation
421 stage than that of wild-type littermates. Interestingly, adult-born NSPCs wield a disproportionately
422 strong influence on DG circuitry and visuospatial learning during younger, but not older, neuronal
423 maturation stages (34). This stage-dependent coupling of NSPC maturation with cognitive outcomes
424 increases the likelihood that accelerated neuronal differentiation rates could negatively impact
425 visuospatial memory acquisition. Furthermore, multispecies comparisons demonstrate that measured
426 decreases in neurogenesis rates are consistent with accelerated neuronal maturation rates across the
427 lifespan (35).

428 The apparent paradox of increased HIF1A activation, despite blunted hypoxia-responsive
429 expression in *Kmt2d*$^{+/\Delta}$ and *Kmt2d*$^{\Delta/\Delta}$ neuronal cells raises two possibilities. First, chronic HIF1A activity
430 could result in cellular compensatory efforts to downregulate hypoxia response genes. In this case,
431 heterochromatin environments at HIF1A-binding genes could prevent induction. Alternatively, cellular
432 oxygen sensing could be coupled to gene expression through chromatin states in a HIF1A-

433 independent manner. Independent studies recently discovered direct oxygen sensing by KDM6A/UTX
434 (the H3K27 demethylase lost in KS2 patients) as well as the H3K4/H3K36 demethylase 5A (KDM5A),
435 which controlled chromatin states and cell differentiation in a HIF1A-independent manner (36, 37).
436 These findings link hypoxia-induced histone methylation at H3K4, H3K27, H3K9, and H3K36 directly
437 with control of maturation in multiple cell types, further supporting the notion that KS-associated
438 transcriptional suppression, in the adult DG context, could impact NSPC stage-dependent learning
439 (34) via metabolic dysregulation. Hypoxia-upregulated H3K4me3 peaks (37) were enriched in HIF1A
440 target gene promoters, where we presently observed high overlaps in KMT2D/HIF1A-bound loci.
441 Strikingly, loss of KDM5A, whose activity opposes that of KMT2D at H3K4 sites, caused upregulation
442 of hypoxia-responsive genes (37), i.e. an effect opposite to the present KS1-associated suppression of
443 hypoxia response genes such as *Klf10* and *Bnip3l.* Several histone demethylases, and at least 33
444 chromatin modifiers in total, have been shown to impact hypoxia response genes, 11 of these
445 associating with developmental disorders or cancers, yet KMT2D and other histone
446 methyltransferases had not yet been implicated (38).
447 In summary, our findings suggest that KMT2D deficiency disrupts neurogenesis by negatively
448 impacting NSPC maintenance functions including cell cycle, proliferation, and survival, accompanied
449 by decreased adult NSPC numbers and precocious neuronal differentiation. Chromatin and
450 transcriptome profiling identified KMT2D- and HIF1A-regulated gene programs suppressed across
451 KS1 model systems, implicating previously described roles for hypoxia responses in regulating
452 neuronal differentiation. Indeed, we functionally demonstrate KMT2D-dependent HIF1A activation and
453 target gene induction in KS1 neural models, and diminished response to hypoxic conditions during in
454 vitro neuronal differentiation in *Kmt2d*$^{+/\beta geo}$ NSPCs. Together, these findings are consistent with an
455 etiological model for KS1-associated developmental changes in which KMT2D loss transcriptionally
456 suppresses oxygen response programs critical to early NSPC maintenance, favoring precocious
457 cellular differentiation during hippocampal neurogenesis.
458

459 **Methods**

460 Media and reagents are listed (**Supplementary Table 10**).

461

462 **Animals**

463 The *Kmt2d*$^{+/\beta geo}$ allele (Mll2Gt(RRt024)Byg) was generated by Bay Genomics (University of
464 California) through the random insertion of a gene trap vector. *Kmt2d*$^{+/\beta geo}$ mice were fully backcrossed
465 to C57Bl/6J background (JAX) over more than 10 generations. Animals were housed in a 14-hour
466 light/10-hour dark cycle with free access to food and water. Experiments compare age- and sex-
467 matched littermates. Genotyping by PCR has been described (12).

468

469 **Primary hippocampal NSPCs**

470 Female C57Bl/6J mice (JAX) were mated to *Kmt2d*$^{+/\beta geo}$ males and sacrificed for embryo
471 harvest at embryonic day 18. Micro-dissected DG from *Kmt2d*$^{+/\beta geo}$ and *Kmt2d*$^{+/+}$ littermate embryos
472 was processed for NSPC isolation and in vitro differentiation as described (39).

473

474 **Patient-derived iPSCs, NSPCs, and fibroblasts**

475 Skin biopsy fibroblasts were cultured from molecularly confirmed KS1 patients (KS1-1, KS1-2,
476 KS1-3). KS1-1 fibroblasts were reprogrammed using non-integrating Sendai virus vectors (CytoTune-
477 iPS 2.0). 5 days post-induction, cells were transferred to mouse embryonic fibroblast (MEF) feeder
478 plates in iPSC media. 21 days post-induction, high quality colonies were manually selected for
479 propagation and karyotyping by G-banding. Generation of healthy control lines (C3-1 and C1-2) was
480 previously described (29). Feeder MEFs from E13.5 CF-1 mice were mitotically inactivated by
481 irradiation. iPSCs were enzymatically passaged every 4-8 days using collagenase. NSPCs were
482 induced from iPSCs as previously described (30), briefly, by inhibiting glycogen synthase kinase 3
483 (GSK3), transforming growth factor β (TGF-β), γ-secretase, and Notch signaling pathways using small
484 molecules CHIR99021 (4 μM), SB431542 (3 μM), and Compound E (0.1 μM), in the presence of hLIF
485 (10 ng/ml) and ROCK inhibitor (5 μM) for 7 days. NSPCs were split with Accutase and propagated in
486 neural induction medium on a Matrigel.

487

488 **CRISPR-Cas9 deletions in HT22 cells**

489 HT22 mouse hippocampal cells are commercially available, but were a gift of the Goff
490 Laboratory and maintained in HT22 media. sgRNAs targeting two loci spanning the *Kmt2d* SET
491 domain-encoding region, with cut sites in exon 52 and either exon 54 (*Kmt2d*$^{\Delta 1}$) or intron 54 (*Kmt2d*$^{\Delta 2}$),

492 were integrated into Cas9 plasmid (pSpCas9BB-2A-puro v2.0 (PX459)) and delivered to cells at 20%
493 confluency using Lipofectamine 2000 according to manufacturer protocol. After puromycin selection,
494 mutant cells were identified by PCR (primers listed) and clonally expanded. Following Sanger
495 sequencing, a subset of clones appearing heterozygous by PCR, but found to bear strand invasion,
496 were removed from analyses.
497
498 **RNA-seq in HT22 cells: library preparation**
499 Cells were plated at equal density and sampled at 60% confluency. Total RNA was isolated
500 from three biological replicates of *Kmt2d*$^{\Delta/\Delta}$ clones and *Kmt2d*$^{+/+}$ parental cells using Direct-Zol RNA
501 MicroPrep, and libraries were constructed in technical triplicate using NEBNext Poly(A) Magnetic
502 Isolation Module and NEBNext UltraII RNA Library Prep Kit for Illumina, with size selection by AMPure
503 XP beads, according to manufacturer protocols. Library quantification and quality checks were done
504 using KAPA Library Quantification Kit for Illumina, High Sensitivity DNA Kit on BioAnalyzer, and Qubit
505 dsDNA HS Assay. Paired end 50 bp reads were obtained for pooled libraries using Illumina HiSeq
506 2500.
507
508 **RNA-seq in HT22 cells: data analysis**
509 We first obtained a fasta file with all mouse cDNA sequences
510 (Mus_musculus.GRCm38.cdna.all.fa.gz) from Ensembl
511 (http://uswest.ensembl.org/Mus_musculus/Info/Index, version 91, downloaded January 2018). Then,
512 sequencing reads were pseudoaligned to this fasta file and transcript abundances were subsequently
513 quantified, using Salmon (40). We then used the tximport R package (41) to convert the transcript
514 abundances into normalized gene-level counts, by setting the "countsFromAbundance" parameter
515 equal to "lengthScaledTPM". Next, we used the edgeR (42, 43) and limma (44) R packages to log2
516 transform these gene-level counts, and normalize each of the samples with the "voom" function using
517 the effective library size (that is, the product of the library size and the normalization factors, the latter
518 of which we computed with the "calcNormFactors" function provided in edgeR). Subsequently, we
519 estimated the mean-variance relationship, and calculated weights for each observation. In order to
520 account for the correlation between technical replicates of the same clone when performing the
521 differential analysis, we fit a mixed linear model, using the function "duplicateCorrelation" from the
522 statmod R package (45) to block on clone. The differential analysis was then performed using the
523 limma R package. Differentially expressed genes were called with 0.05 as the cutoff for the False
524 Discovery Rate (FDR).

525 When performing the principal component analysis, transcript abundances were first converted
526 into gene-level counts using the tximport R package, with the “countsFromAbundance” parameter
527 equal to “no”. Then, we applied a variance stabilizing transformation to these gene-level counts using
528 the “vst” function from the DESeq2 R package (46), with the parameter “blind” set to “TRUE”, and
529 subsequently estimated the principal components (without scaling the expression matrix) using the
530 1000 most variable genes.
531
532 **scRNA-seq: library preparation**
533 NSPCs were induced in parallel from each iPSC line (KS1-1, C1-2, C3-1) under identical conditions,
534 and passaged three times before sampling. iPSCs were detached from MEF feeders using
535 collagenase (200 units/ml). iPSCs and NSPCs were dissociated to single-cell suspension using
536 Accutase. Cell counts and viability were analyzed using Countess II. scRNA-seq libraries were created
537 with Chromium Single Cell 3’ Library & Gel Bead Kit v2 (10x Genomics) according to manufacturer
538 protocol. Targeted cell recovery for each sample was 5,000 cells. Sufficient cDNA for library
539 construction was achieved using 20 amplification cycles for iPSC libraries and 16 cycles for NSPC
540 libraries. Sample indexing was achieved using 11 PCR cycles for iPSC libraries and 5 cycles for NSPC
541 libraries. scRNA-seq libraries were sequenced using Illumina NextSeq 500.
542
543 **scRNA-seq: data analysis**
544 Sequencing output was processed through the Cell Ranger 2.1.0 preprocessing pipeline using default
545 parameters with the exception of --expect-cells=5000 for `cellranger count` and --normalize=none for
546 `cellranger aggr`. Reads were quantified against hg19 using the 10x reference genome and
547 transcriptome builds (refdata-cellranger-GRCh38-1.2.0). The aggregated raw count matrix was then
548 used as input for the Monocle2 single-cell RNAseq framework. Differential gene expression analysis
549 was performed on all NSPCs and iPSCs with respect to genotype (KS1 patient vs healthy control) and
550 was performed using the Monocle2 (47) likelihood ratio test (0.1% FDR, Monocle2 LRT, Benjamini-
551 Hochberg corrected) with `num_genes_expressed` added as a nuisance parameter to both the full and
552 reduced models. The directionality of the differential gene test was determined by calculating the
553 mean gene expression across all KS1 patient-derived and healthy control cells respectively, evaluating
554 the relative fold change. High-variance genes were selected as those with a positive residual to the
555 estimated dispersion fit and a mean number of reads per cell >=0.0005. Cell cycle stage was
556 determined by profiling cell cycle associated genes across all cells and assigning cell cycle state using
557 the R/Bioconductor package scran (48). Dimensionality reduction and visualization was performed via

558 UMAP (31) on the log10(counts + 1) of the high variance genes in the NSPC dataset. The first 10
559 principal components were used as input for UMAP using the default parameters of the R/CRAN
560 package umap. Cells were assigned to clusters using Monocle2's implementation of the louvain
561 community detection algorithm. Learned clusters were then aggregated by hand based on marker
562 gene expression into three clusters ("Differentiating", "Transitioning", "Cycling"). Differential gene
563 expression within clusters, and between genotypes was performed as described above. The
564 "Differentiating" cluster was then segregated, and a smooth line was fitted using a linear regression.
565 This line was determined to represent the direction of differentiation by examination of marker genes
566 (**Supplementary Figure 5C-H**). The residuals of this fit were then plotted and deciles were calculated
567 containing equal number of cells along the axis of differentiation. The number of cells in each decile
568 was then counted with respect to genotype.
569
570 **ChIP-seq: library preparation**
571 *Kmt2d*$^{+/+}$ HT22 cells were sampled at 70% confluency and processed for pull-down with ChIP-grade
572 KMT2D antibody (Millipore Sigma) according to ENCODE guidelines. Sonicated, reverse-crosslinked
573 chromatin served as input control. Briefly, ~300 million cells per cell line were crosslinked in 1%
574 formaldehyde, quenched with 0.125 M glycine, and cell lysate supernatants were collected for
575 immediate processing or snap-frozen for storage at -80°C. Nuclei (20 million/sample) were diluted in 1
576 ml RIPA buffer were sonicated using Bioruptor for 6 cycles of 5 minutes (60 seconds on/30 seconds
577 off) in ice-cold water bath. Supernatants containing sheared chromatin were pre-cleared with Protein
578 A Dynabeads and incubated overnight at 4°C with 8 µg KMT2D antibody. ChIP DNA was recovered by
579 Dynabead incubation (overnight at 4°C plus 6 hours at room temperature) before 6 sequential salt
580 washes of increasing stringency, then eluted and reverse crosslinked overnight at 65°C. DNA was
581 purified using DNA Clean and Concentrator (Zymo Research) and quantified using High Sensitivity
582 DNA Kit on BioAnalyzer, and Qubit dsDNA HS Assay. DNA libraries were constructed using NEBNext
583 UltraII DNA Library Prep Kit for Illumina and quantified using KAPA Library Quantification Kit for
584 Illumina. Paired end 75 bp reads were obtained for pooled libraries using Illumina HiSeq 2500.
585
586 **ChIP-seq: data analysis**
587 Sequencing reads were aligned to the mouse reference genome (mm10) using Bowtie2 (49). Then,
588 duplicate reads were removed with the function MarkDuplicates from Picard
589 (http://broadinstitute.github.io/picard/). Peaks were subsequently called using MACS2 (50), with the
590 "keep-dup" parameter equal to "all". After peak calling, we excluded all peaks that overlapped with

591 blacklisted regions provided by ENCODE (51). As a quality metric, using the resulting list of peaks, we
592 computed the fraction of reads in peaks (frip) with the "featureCounts" function in the Rsubread
593 package (52), with the "requireBothEndsMapped" parameter equal to "TRUE", and the
594 "countChimericFragments" and "countMultiMappingReads" parameters equal to FALSE. We found
595 frip to be 2.9%, which is within the typically encountered range of values for a point-source factor (53).
596 To identify genes likely to be regulated in *cis* by KMT2D, we first obtained the coordinates of 10kb
597 regions centered around the TSS for each gene, using the "promoters" function from the
598 EnsDb.Mmusculus.v79 R package (54), with the "filter" parameter equal to
599 "TxBiotypeFilter("protein_coding")", and the "upstream" and "downstream" parameters both equal to
600 5000. Subsequently, we selected those genes whose extended promoter (+/- 5kb from the TSS)
601 overlapped with at least one KMT2D peak, using the "findOverlaps" function in the GenomicRanges R
602 package (55).
603
604 **Purification of EdU$^+$ nuclei**
605 Mice were given 150 mg/kg EdU by intraperitoneal injection and sampled after 16 hours. DG was
606 micro-dissected in ice-cold PBS immediately following sacrifice by halothane inhalation. Total nuclei
607 were purified as described (56) with addition of RNase inhibitor to all buffers. Briefly, DG was dounce-
608 homogenized in 1 ml lysis buffer and layered above a sucrose gradient for ultracentrifugation at
609 28,600 RPM for 2 hours at 4°C. Nuclei were resuspended in Click-iT EdU AlexaFluor-488 with RNAse
610 inhibitor, and incubated 30 minutes at room temperature. Samples were passed through 40 µm filter,
611 stained with 1 µg/ml DAPI, and kept on ice before sorting. Lysates processed identically from non-
612 EdU-injected mice served as negative controls during sorting with Beckman Coulter MoFlo Cell Sorter.
613 Cell cycle analysis by DNA content was performed with gates discriminating 2N and 4N cells by DAPI
614 fluorescence.
615
616 **RNA-seq: EdU$^+$ nuclei**
617 Purified EdU$^+$ nuclei from 3 *Kmt2d*$^{+/\beta geo}$ and 3 wild-type littermate female mice (500 nuclei pooled per
618 genotype) were sorted into Smart-Seq 2 lysis buffer (2 µL Smart-Seq2 lysis buffer with RNase
619 inhibitor, 1 µL oligo-dT primer, and 1 µL dNTPs), briefly spun by tabletop microcentrifuge, and snap-
620 frozen on dry ice. Nuclei were processed according to a modified Smart-seq2 protocol (57). Briefly,
621 lysates were thawed to 4°C, heated to 72°C for 5 minutes, and immediately placed on ice. Template-
622 switching first-strand cDNA synthesis was performed using a 5'-biotinylated TSO oligo. cDNAs were
623 amplified using 20 cycles of KAPA HiFi PCR and 5'-biotinylated ISPCR primer. Amplified cDNA was

624 cleaned using 1:1 ratio of Ampure XP beads and approximately 250 pg was input to a one-quarter-
625 sized Nextera XT tagmentation reaction. Tagmented fragments were amplified for 12 enrichment
626 cycles and dual indexes were added to each well to uniquely label each library. Concentrations were
627 assessed with Quant-iT PicoGreen dsDNA Reagent (Invitrogen) and samples were diluted to ~2nM
628 and pooled. Pooled libraries were sequenced on the Illumina HiSeq 2500 platform to a target mean
629 depth of ~8 x 105 bp paired-end fragments per cycle. Paired-end reads were aligned to mm10 using
630 HISAT2 (58) with default parameters except: -p 8. Aligned reads from individual samples were
631 quantified against a reference genome (GENCODE vM8) using cuffquant (59). Normalized expression
632 estimates across all samples were obtained using cuffnorm with default parameters (60).
633
634 **RT-qPCR**
635 Total RNA was isolated by RNeasy Mini and cDNA libraries were constructed with High-Capacity
636 cDNA Reverse Transcription Kit (Applied Biosystems) according to manufacturer protocols.
637 Experiments were performed in technical triplicate, with biological replicates as indicated. Probes
638 were from Taqman.
639
640 **Immunostaining, confocal imaging, and processing**
641 Coronal brain sections of 30 μm (every sixth slice) were analyzed in serial order. Briefly, adult brains
642 were PFA-fixed by transcardial perfusion and post-fixed for 12 hours before cryoprotection by 30%
643 sucrose in phosphate buffer. Brains were sectioned by cryostat (Leica), directly mounted to charged
644 slides, and stored at -80°C. Antigen retrieval (DakoCytomation) was performed at 95°C for 20 minutes.
645 Overnight incubation at 4°C in primary antibodies (**Supplementary Table 10**) preceded AlexaFluor-
646 conjugated secondary antibody (1:500). Tiled, z-stacked images were acquired using Zeiss LSM780
647 FCS AxioObserver confocal microscope and Zen software (Zeiss) to encompass entire DG structure.
648 Images were quantified using Imaris (BitPlane) by experimenters blinded to genotype. Cell counts
649 were corrected by DG area multiplied by z-thickness, and expressed as cells/mm^3. For pulse-label
650 experiments, mice were injected with 150 mg/kg EdU in saline every 48 hours and sampled as above.
651 DCX^+ neuroblast distance from SGZ plane was measured in Fiji (NIH). Patient-derived cell imaging
652 utilized EVOS FL Cell Imaging System with analysis in Fiji.
653
654 **FACS and analysis**
655 Flow cytometry analysis with FACSverse and FACSsuite (BD Biosciences), and sorting by Beckman
656 Coulter MoFlo Cell Sorter with proper gate settings and doublet discrimination (**Supplementary**

657 **Figure 3J, Supplementary Figure 6A**). Runs of 10,000 or more cells were analyzed from technical
658 triplicate culture wells and analyzed in FlowJo v10 (Tree Star Inc). Unstained and secondary-only
659 samples served as control. Cells were sampled after 30-minute pulse of EdU (10 μM) using Click-iT
660 EdU Flow Cytometry Assay (ThermoFisher Scientific). CellTrace Violet and CellEvent caspase-3/7
661 reagent (ThermoFisher Scientific) were used according to manufacturer protocols. For cycle
662 synchronization, 250 ng/ml nocodazole (Sigma) was applied for 18 hours before release.
663
664 **Magnetic Resonance Imaging (MRI)**
665 3D T2-weighted MRI (9.4T) was performed in PFA-perfused brains of *Kmt2d*$^{+/\beta geo}$ (n=3) and *Kmt2d*$^{+/+}$
666 (n=3) female mice aged 4 months. Atlas-based, volume-corrected analysis was performed in 25 brain
667 regions (DtiStudio).
668
669 **Statistics**
670 For high-throughput experiments, see Methods. For cellular assays, see Figure Legends. Statistical
671 analyses with multiple comparisons correction were done with GraphPad Prism (version 7.0b). Gene
672 set enrichments were determined according to WebGestalt (61), or by Fisher's Exact Test in R version
673 3.5.2 as indicated.
674
675 **Study Approval**
676 All mouse experiments were performed using protocols approved by the Animal Care and Use
677 Committee of Johns Hopkins University School of Medicine and are in accordance with NIH
678 guidelines. Informed consent regarding KS1 patient samples was obtained according to institutional
679 IRB and ISCRO protocols approved by JHU.
680
681 **Author contributions**
682 GAC and HTB conceived the study; GAC and HTB wrote the manuscript; GAC, HNN, GC, JDR, LZ
683 performed experiments; GAC, LB, JA, KDH and LG analyzed data.
684
685 **Acknowledgments**
686 HTB is funded through an Early Independence Award from the National Institutes of Health (NIH,
687 DP5OD017877), the Icelandic Research Fund (195835-051), and the Louma G. Foundation. Imaging
688 was performed with NIH support (S10OD016374). Karyotype facility supported by NICHD (1U54
689 HD079123-01A1). FACS was performed at the Bloomberg School of Public Health. We thank Michael

690 Sherman for assistance with image quantification and Manisha Aggarwal for MRI. Schematics created
691 with Mark Sandusky or Biorender.com. Hongjun Song and Kai Ge provided critical reagents and
692 advice. Hal Dietz and Gregg Semenza provided conceptual guidance.
693
694 **Data availability**
695 High-throughput data are publicly available. RNA-seq and ChIP-seq: GEO #GSE126167. scRNA-seq:
696 GEO #GSE126027. Scripts for scRNA-seq analysis are available at
697 https://github.com/Jaugust7/Kabuki-Syndrome-scRNA-analysis.

References

1. Schuettengruber B, Bourbon H-M, Di Croce L, Cavalli G. Genome regulation by polycomb and trithorax: 70 years and counting.. *Cell* 2017;171(1):34–57.
2. Bjornsson HT. The Mendelian disorders of the epigenetic machinery.. *Genome Res.* 2015;25(10):1473–1481.
3. Ng SB et al. Exome sequencing identifies MLL2 mutations as a cause of Kabuki syndrome.. *Nat. Genet.* 2010;42(9):790–793.
4. Miyake N et al. KDM 6 A Point Mutations Cause K abuki Syndrome.. *Human mutation* 2013;34(1):108–110.
5. Hannibal MC et al. Spectrum of MLL2 (ALR) mutations in 110 cases of Kabuki syndrome.. *Am. J. Med. Genet. A* 2011;155A(7):1511–1516.
6. Ang S-Y et al. KMT2D regulates specific programs in heart development via histone H3 lysine 4 di-methylation.. *Development* 2016;143(5):810–821.
7. Ortega-Molina A et al. The histone lysine methyltransferase KMT2D sustains a gene expression program that represses B cell lymphoma development.. *Nat. Med.* 2015;21(10):1199–1208.
8. Zhang J et al. Disruption of KMT2D perturbs germinal center B cell development and promotes lymphomagenesis.. *Nat. Med.* 2015;21(10):1190–1198.
9. Lee J-E et al. H3K4 mono- and di-methyltransferase MLL4 is required for enhancer activation during cell differentiation.. *Elife* 2013;2:e01503.
10. Lin-Shiao E et al. KMT2D regulates p63 target enhancers to coordinate epithelial homeostasis.. *Genes Dev.* 2018;32(2):181–193.
11. Froimchuk E, Jang Y, Ge K. Histone H3 lysine 4 methyltransferase KMT2D.. *Gene* 2017;627:337–342.
12. Bjornsson HT et al. Histone deacetylase inhibition rescues structural and functional brain deficits in a mouse model of Kabuki syndrome.. *Sci Transl Med* 2014;6(256):256ra135.
13. Boisgontier J et al. Anatomical and functional abnormalities on MRI in kabuki syndrome.. *Neuroimage Clin.* [published online ahead of print: November 19, 2018]; doi:10.1016/j.nicl.2018.11.020
14. Gonçalves JT, Schafer ST, Gage FH. Adult neurogenesis in the hippocampus: from stem cells to behavior.. *Cell* 2016;167(4):897–914.
15. Moreno-Jiménez EP et al. Adult hippocampal neurogenesis is abundant in neurologically healthy subjects and drops sharply in patients with Alzheimer's disease.. *Nat. Med.* 2019;25(4):554–560.
16. Tobin MK et al. Human hippocampal neurogenesis persists in aged adults and alzheimer's disease patients.. *Cell Stem Cell* 2019;24(6):974–982.e3.
17. Sorrells SF et al. Human hippocampal neurogenesis drops sharply in children to undetectable levels in adults.. *Nature* 2018;555(7696):377–381.
18. Berg DA et al. A common embryonic origin of stem cells drives developmental and adult neurogenesis.. *Cell* 2019;177(3):654–668.e15.
19. Zheng X et al. Metabolic reprogramming during neuronal differentiation from aerobic glycolysis to neuronal oxidative phosphorylation.. *Elife* 2016;5. doi:10.7554/eLife.13374
20. Mazumdar J et al. O2 regulates stem cells through Wnt/β-catenin signalling.. *Nat. Cell Biol.* 2010;12(10):1007–1013.
21. Chatzi C, Schnell E, Westbrook GL. Localized hypoxia within the subgranular zone determines the early survival of newborn hippocampal granule cells.. *Elife* 2015;4:e08722.
22. Morimoto BH, Koshland DE. Induction and expression of long- and short-term neurosecretory potentiation in a neural cell line.. *Neuron* 1990;5(6):875–880.
23. Wang C et al. Enhancer priming by H3K4 methyltransferase MLL4 controls cell fate transition..

744 *Proc. Natl. Acad. Sci. USA* 2016;113(42):11871–11876.
745 24. Guo C et al. Global identification of MLL2-targeted loci reveals MLL2's role in diverse signaling
746 pathways.. *Proc. Natl. Acad. Sci. USA* 2012;109(43):17603–17608.
747 25. Semenza GL. HIF-1: mediator of physiological and pathophysiological responses to hypoxia.. *J.*
748 *Appl. Physiol.* 2000;88(4):1474–1480.
749 26. Guimarães-Camboa N et al. Hif1α represses cell stress pathways to allow proliferation of hypoxic
750 fetal cardiomyocytes.. *Dev. Cell* 2015;33(5):507–521.
751 27. Benita Y et al. An integrative genomics approach identifies Hypoxia Inducible Factor-1 (HIF-1)-
752 target genes that form the core response to hypoxia.. *Nucleic Acids Res.* 2009;37(14):4587–4602.
753 28. Sanz JH, Lipkin P, Rosenbaum K, Mahone EM. Developmental profile and trajectory of
754 neuropsychological skills in a child with Kabuki syndrome: implications for assessment of syndromes
755 associated with intellectual disability.. *Clin Neuropsychol* 2010;24(7):1181–1192.
756 29. Wen Z et al. Synaptic dysregulation in a human iPS cell model of mental disorders.. *Nature*
757 2014;515(7527):414–418.
758 30. Li W et al. Rapid induction and long-term self-renewal of primitive neural precursors from human
759 embryonic stem cells by small molecule inhibitors.. *Proc. Natl. Acad. Sci. USA* 2011;108(20):8299–
760 8304.
761 31. McInnes L, Healy J, Saul N, Großberger L. UMAP: uniform manifold approximation and projection.
762 *JOSS* 2018;3(29):861.
763 32. Benjamin JS et al. A ketogenic diet rescues hippocampal memory defects in a mouse model of
764 Kabuki syndrome.. *Proc. Natl. Acad. Sci. USA* 2017;114(1):125–130.
765 33. Morris AM, Churchwell JC, Kesner RP, Gilbert PE. Selective lesions of the dentate gyrus produce
766 disruptions in place learning for adjacent spatial locations.. *Neurobiol. Learn. Mem.* 2012;97(3):326–
767 331.
768 34. Zhuo J-M et al. Young adult born neurons enhance hippocampal dependent performance via
769 influences on bilateral networks.. *Elife* 2016;5. doi:10.7554/eLife.22429
770 35. Snyder JS. Recalibrating the relevance of adult neurogenesis.. *Trends Neurosci.* 2019;42(3):164–
771 178.
772 36. Chakraborty AA et al. Histone demethylase KDM6A directly senses oxygen to control chromatin
773 and cell fate.. *Science (80-.).* 2019;363(6432):1217–1222.
774 37. Batie M et al. Hypoxia induces rapid changes to histone methylation and reprograms chromatin..
775 *Science (80-.).* 2019;363(6432):1222–1226.
776 38. Luo W, Wang Y. Epigenetic regulators: multifunctional proteins modulating hypoxia-inducible
777 factor-α protein stability and activity.. *Cell Mol. Life Sci.* 2018;75(6):1043–1056.
778 39. Bernas S, Leiter O, Walker T, Kempermann G. Isolation, culture and differentiation of adult
779 hippocampal precursor cells. *Bio Protoc* 2017;7(21). doi:10.21769/BioProtoc.2603
780 40. Patro R, Duggal G, Love MI, Irizarry RA, Kingsford C. Salmon provides fast and bias-aware
781 quantification of transcript expression.. *Nat. Methods* 2017;14(4):417–419.
782 41. Soneson C, Love MI, Robinson MD. Differential analyses for RNA-seq: transcript-level estimates
783 improve gene-level inferences. [version 2; peer review: 2 approved]. *F1000Res.* 2015;4:1521.
784 42. Robinson MD, McCarthy DJ, Smyth GK. edgeR: a Bioconductor package for differential expression
785 analysis of digital gene expression data.. *Bioinformatics* 2010;26(1):139–140.
786 43. McCarthy DJ, Chen Y, Smyth GK. Differential expression analysis of multifactor RNA-Seq
787 experiments with respect to biological variation.. *Nucleic Acids Res.* 2012;40(10):4288–4297.
788 44. Ritchie ME et al. limma powers differential expression analyses for RNA-sequencing and
789 microarray studies.. *Nucleic Acids Res.* 2015;43(7):e47.

790 45. Giner G, Smyth GK. Statmod: probability calculations for the inverse Gaussian distribution.. *arXiv*
791 *preprint arXiv:1603.06687* 2016;
792 46. Love MI, Huber W, Anders S. Moderated estimation of fold change and dispersion for RNA-seq
793 data with DESeq2.. *Genome Biol.* 2014;15(12):550.
794 47. Trapnell C et al. The dynamics and regulators of cell fate decisions are revealed by pseudotemporal
795 ordering of single cells.. *Nat. Biotechnol.* 2014;32(4):381–386.
796 48. Lun ATL, McCarthy DJ, Marioni JC. A step-by-step workflow for low-level analysis of single-cell
797 RNA-seq data with Bioconductor. [version 2; peer review: 3 approved, 2 approved with reservations].
798 *F1000Res.* 2016;5:2122.
799 49. Langmead B, Salzberg SL. Fast gapped-read alignment with Bowtie 2.. *Nat. Methods*
800 2012;9(4):357–359.
801 50. Zhang Y et al. Model-based analysis of ChIP-Seq (MACS).. *Genome Biol.* 2008;9(9):R137.
802 51. Amemiya HM, Kundaje A, Boyle AP. The ENCODE blacklist: identification of problematic regions
803 of the genome.. *Sci. Rep.* 2019;9(1):9354.
804 52. Liao Y, Smyth GK, Shi W. The R package Rsubread is easier, faster, cheaper and better for
805 alignment and quantification of RNA sequencing reads.. *Nucleic Acids Res.* 2019;47(8):e47.
806 53. Landt SG et al. ChIP-seq guidelines and practices of the ENCODE and modENCODE consortia..
807 *Genome Res.* 2012;22(9):1813–1831.
808 54. Rainer. EnsDb.Mmusculus.v79: Ensembl based annotation package.. *R package version 2.99.0.*
809 2017;
810 55. Lawrence M et al. Software for computing and annotating genomic ranges.. *PLoS Comput. Biol.*
811 2013;9(8):e1003118.
812 56. Rizzardi LF et al. Neuronal brain-region-specific DNA methylation and chromatin accessibility are
813 associated with neuropsychiatric trait heritability.. *Nat. Neurosci.* 2019;22(2):307–316.
814 57. Picelli S et al. Smart-seq2 for sensitive full-length transcriptome profiling in single cells.. *Nat.*
815 *Methods* 2013;10(11):1096–1098.
816 58. Kim D, Langmead B, Salzberg SL. HISAT: a fast spliced aligner with low memory requirements..
817 *Nat. Methods* 2015;12(4):357–360.
818 59. Mudge JM, Harrow J. Creating reference gene annotation for the mouse C57BL6/J genome
819 assembly.. *Mamm. Genome* 2015;26(9–10):366–378.
820 60. Trapnell C et al. Differential gene and transcript expression analysis of RNA-seq experiments with
821 TopHat and Cufflinks.. *Nat. Protoc.* 2012;7(3):562–578.
822 61. Wang J, Vasaikar S, Shi Z, Greer M, Zhang B. WebGestalt 2017: a more comprehensive, powerful,
823 flexible and interactive gene set enrichment analysis toolkit.. *Nucleic Acids Res.* 2017;45(W1):W130–
824 W137.
825
826
827

Figures

Figure 1. Genetic ablation of the *Kmt2d* SET methyltransferase domain disrupts proliferation and cell cycle in a cell-autonomous manner.

Figure 2. Suppressed transcription of KMT2D-regulated hypoxia response genes upon loss of the *Kmt2d* SET methyltransferase domain in neuronal cells.

Figure 3. KS1 patient-derived cells recapitulate KMT2D-associated defects in proliferation and cell cycle.

Figure 4. Transcriptional suppression of metabolic genes in cycling cells, and precocious neuronal differentiation in KS1 patient-derived NSPCs.

Figure 5. In vivo defects of neurogenesis and NSPC differentiation in a *Kmt2d*$^{+/\beta geo}$ mouse model of KS1

Supplementary Figures

Supplementary Figure 1: CRISPR-targeted HT22 cells

Supplementary Figure 2: HT22 cell RNA-seq and ChIP-seq analysis

Supplementary Figure 3: iPSC and NSPC validations and phenotyping

Supplementary Figure 4: iPSC and NSPC single-cell RNA-seq analysis

Supplementary Figure 5. Stratified scRNA-seq analysis of NSPCs

Supplementary Figure 6: Adult neurogenesis phenotypes in *Kmt2d*$^{+/\beta geo}$ mice

Supplementary Figure 7: Pulse-labeling to birth-date adult-born NSPCs in vivo

Supplementary Figure 8: Comparison of gene expression across KS1 models

Supplementary Figure 9: HIF1A activation in primary hippocampal NSPCs

Supplementary Figure 10: Precocious in vitro differentiation of primary hippocampal NSPCs

Supplementary Tables

Supplementary Table 1: Differentially expressed genes in HT22 cells (*Kmt2d*$^{+/+}$ versus *Kmt2d*$^{\Delta/\Delta}$)

Supplementary Table 2: KMT2D ChIP-seq peaks in HT22 cells (*Kmt2d*$^{+/+}$ cells)

Supplementary Table 3: KMT2D-bound genes in HT22 cells (*Kmt2d*$^{+/+}$ cells)

Supplementary Table 4: Differentially expressed genes in iPSCs (KS1 versus controls)

Supplementary Table 5: Differentially expressed genes in NSPCs (KS1 versus controls)

Supplementary Table 6: Intersected gene sets of iPSCs and NSPCs

Supplementary Table 7: Differentially expressed genes in NSPCs (stratified by subsets)

Supplementary Table 8: Differentially expressed genes in EdU^{+} DG nuclei of *Kmt2d*$^{+/\beta geo}$ mice

Supplementary Table 9: MRI volumetric comparisons in wild-type and *Kmt2d*$^{+/\beta geo}$ mice

Supplementary Table 10: Reagents

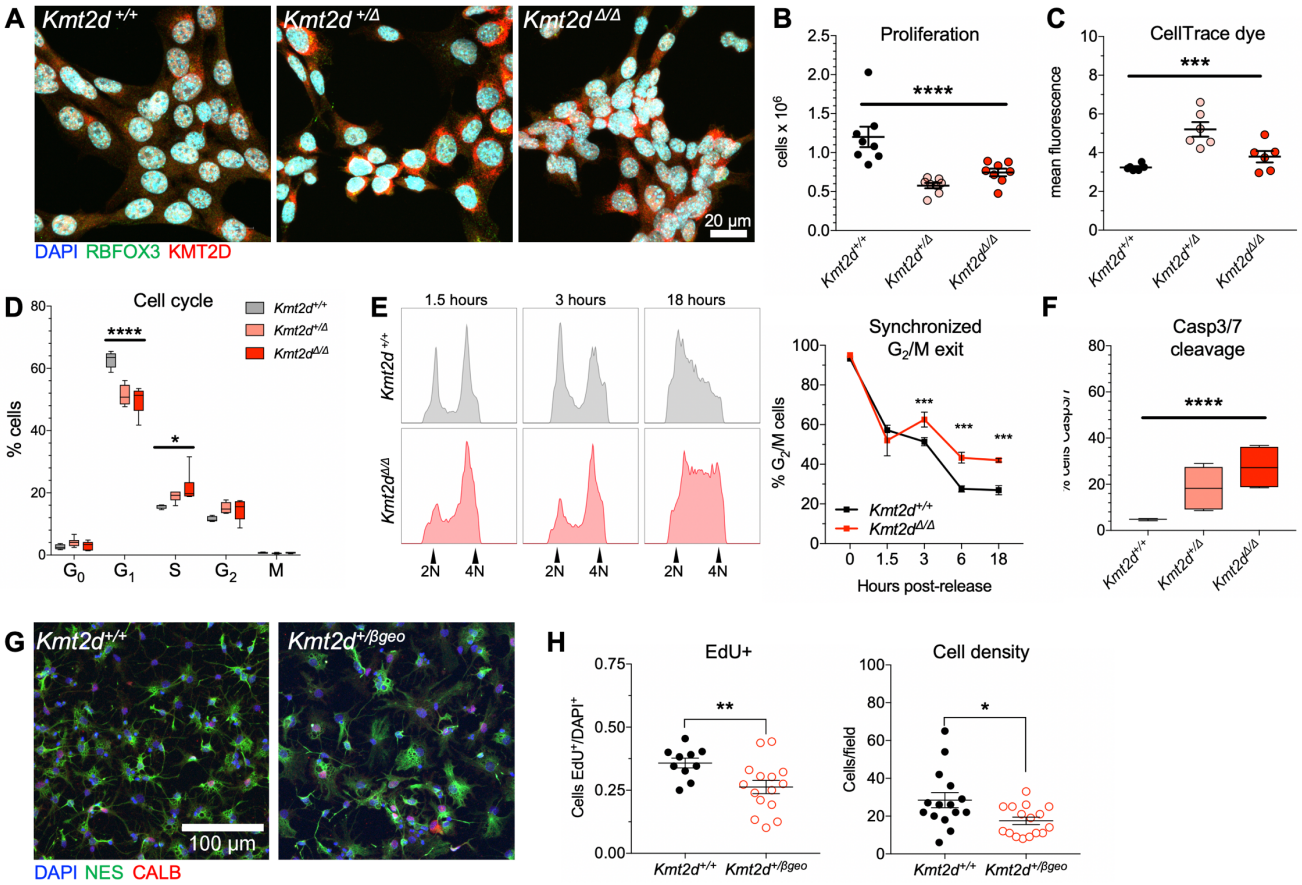

Figure 1. Genetic ablation of the *Kmt2d* SET methyltransferase domain disrupts proliferation and cell cycle in a cell-autonomous manner. (**A**) Representative immunostaining against KMT2D and RBFOX3 in *Kmt2d*$^{+/+}$, *Kmt2d*$^{+/\Delta}$, and *Kmt2d*$^{\Delta/\Delta}$ HT22 cells. (**B**) Decreased proliferation in *Kmt2d*-inactivated cells quantified 72 hours after equal density plating. One-way ANOVA. (**C**) Generational tracking reveals fewer cell divisions, i.e. reduced dye dilution, of CellTrace Violet in *Kmt2d*$^{+/\Delta}$ and *Kmt2d*$^{\Delta/\Delta}$ cells at 72 hours. One-way ANOVA. (**D**) Flow cytometric quantification of cell cycle phases using KI67 and DAPI fluorescence. One-way ANOVA for each cycle phase, independently. (**E**) *Kmt2d*$^{+/+}$ and *Kmt2d*$^{\Delta/\Delta}$ cells synchronized and released for analysis of G_2/M exit, by DNA content, up to 18 hours after release, and quantification of cells in G_2/M (technical triplicates per time point). Bars indicate mean ± SEM. Two-way ANOVA ($P<0.0001$) with post hoc multiple comparisons. (**F**) Flow cytometric quantification of early apoptotic cells by caspase-3/7 fluorescence. One-way ANOVA. (**G**) Confocal images of nestin (NES) and calbindin (CALB) expressing primary hippocampal NSPCs from *Kmt2d*$^{+/+}$ and *Kmt2d*$^{+/\beta geo}$ mice, and (**H**) quantified proliferation. Student's t-test. Bars indicate mean ± SEM. Boxes indicate mean ± interquartile range; whiskers indicate minima and maxima. (*$p<0.05$, **$p<0.01$, ***$p<0.001$, ****$p<0.0001$). Scale bars 20 µm (**A**) or 100 µm (**G**).

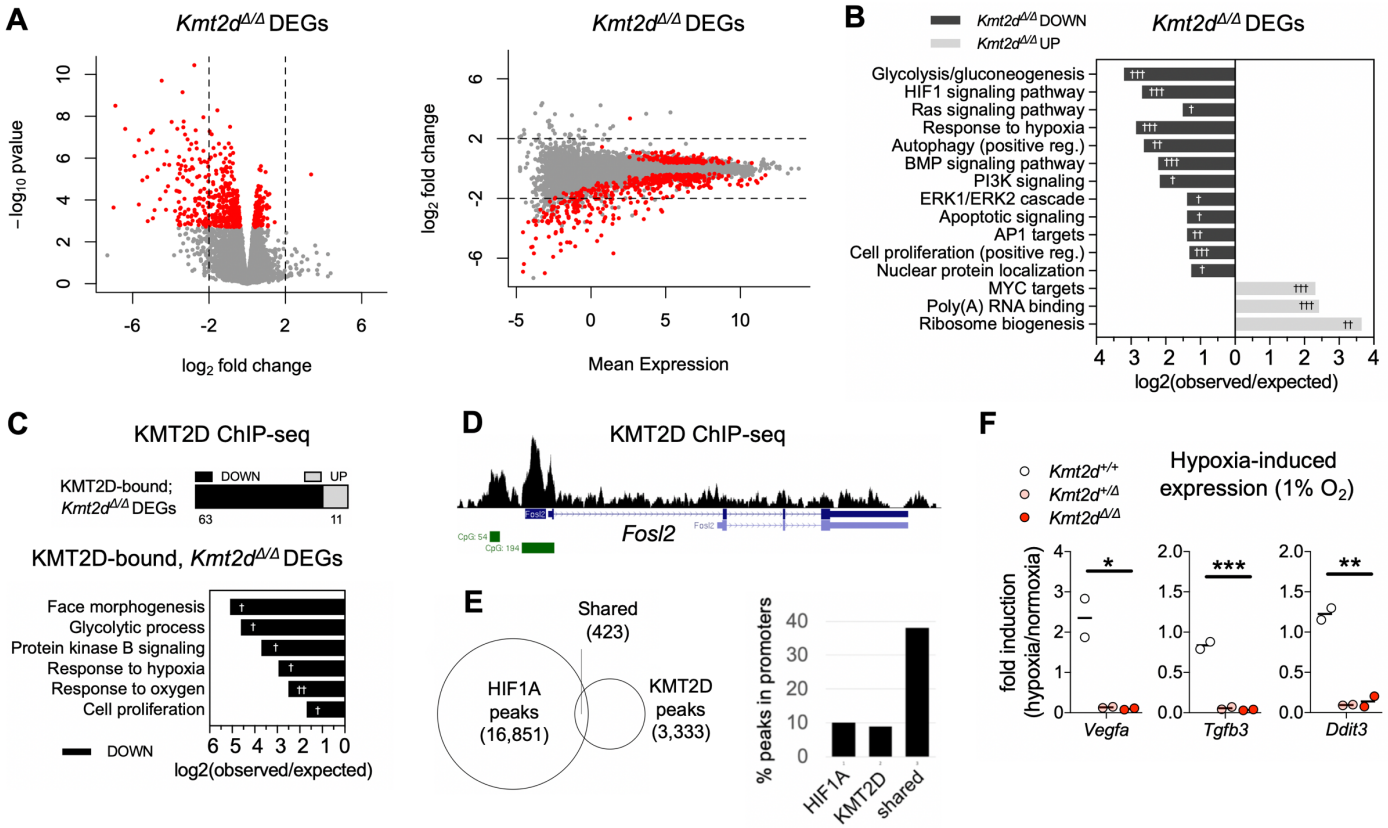

Figure 2. Suppressed transcription of KMT2D-regulated hypoxia response genes upon loss of the *Kmt2d* SET methyltransferase domain in neuronal cells. (**A**) Expression analysis by RNA-seq in HT22 cells reveals 575 significant differentially expressed genes (DEGs) in *Kmt2d*$^{\Delta/\Delta}$ clones (3 biological replicates) relative to *Kmt2d*$^{+/+}$ cells, each in technical triplicate. Fold changes in expression indicate most significant *Kmt2d*$^{\Delta/\Delta}$ DEGs (~76%, red dots) are downregulated in *Kmt2d*$^{\Delta/\Delta}$ cells, plotted against p-value and mean expression. (**B**) Gene networks significantly enriched among down- or up-regulated *Kmt2d*$^{\Delta/\Delta}$ DEGs. (**C**) *Kmt2d*$^{\Delta/\Delta}$ DEGs which are also KMT2D-bound, as determined by ChIP-seq chromatin profiling in *Kmt2d*$^{+/+}$ HT22 cells, and gene networks significantly enriched among KMT2D-bound, *Kmt2d*$^{\Delta/\Delta}$ DEGs. (**D**) Representative ChIP-seq track of a KMT2D-bound, *Kmt2d*$^{\Delta/\Delta}$ DEG depicting KMT2D binding peaks (black), RefSeq gene annotations (blue), and CpG islands (green). (**E**) Overlapping loci of observed KMT2D-ChIP peaks in HT22 cells and HIF1A-ChIP peaks in embryonic heart (26). Overlapping KMT2D/HIF1A peak regions, compared to individually bound regions, are enriched at gene promoters. (**F**) RT-qPCR analysis of hypoxia-induced gene expression in *Kmt2d*$^{+/+}$, *Kmt2d*$^{+/\Delta}$, and *Kmt2d*$^{\Delta/\Delta}$ cells, following 72 hours in normoxia (21% O_2) or hypoxia (1% O_2), with fold induction of target gene mRNA. 2 biological replicates per genotype, each in technical triplicate. One-way ANOVA. (*p<0.05, **p<0.01, ***p<0.001). Fisher's Exact Test (†FDR<0.05, ††FDR<0.01, †††FDR<0.001).

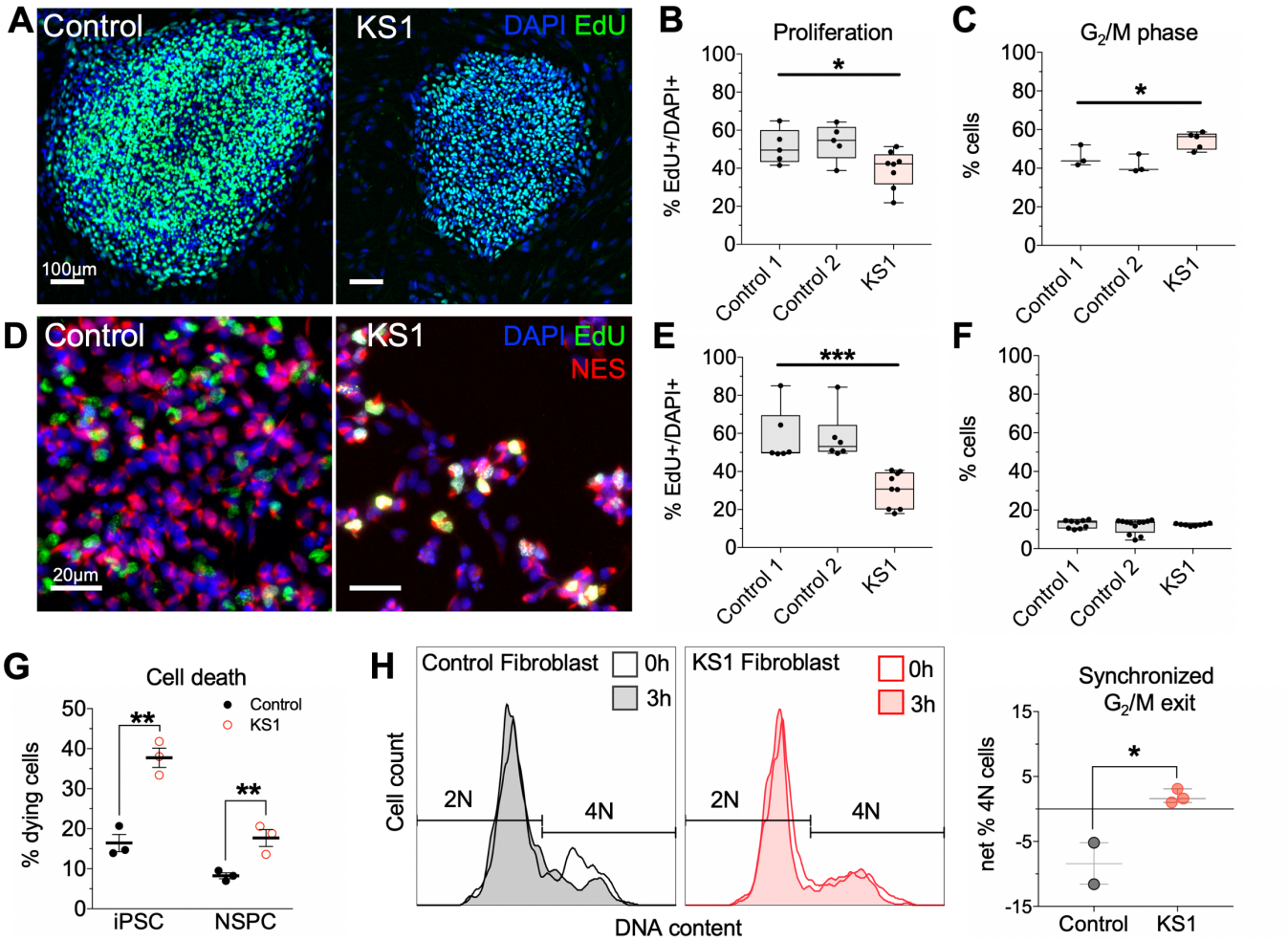

Figure 3. KS1 patient-derived cells recapitulate KMT2D-associated defects in proliferation and cell cycle. (**A**) Representative immunostaining of iPSCs derived from a *KMT2D*$^{+/-}$ KS1 patient (c.7903C>T:p.R2635*) and healthy controls. (**B**) Proliferating cells were pulsed with EdU for 30 minutes and quantified by flow cytometry. One-way ANOVA. (**C**) Cell cycle analysis in iPSCs, discriminating 2N and 4N DNA content (G_1/G_0 and G_2/M, respectively) by flow cytometry using DAPI fluorescence. One-way ANOVA. (**D**) Representative immunostaining of NES-expressing NSPCs induced from iPSCs of KS1 patient and controls. (**E**) EdU pulse assay quantified by flow cytometry. One-way ANOVA. (**F**) Cell cycle analysis in NSPCs. One-way ANOVA. (**G**) Quantification of dying cells by flow cytometric scatter profiles in KS1 patient and control cells. Student's t-test. (**H**) Synchronized G_2/M exit analysis by flow cytometry in fibroblasts from KS1 patients (KS1-1, KS1-2, KS1-3) and healthy controls (Controls 3 and 4), in triplicate per cell line. Cells were enriched for G_2/M phase using nocodazole and analyzed by DAPI fluorescence to quantify G_2/M phase cell fractions at 0 and 3 hours after release. Student's t-test. Bars indicate mean ± SEM. Boxes indicate mean ± interquartile range; whiskers indicate minima and maxima. (*$p<0.05$, **$p<0.01$, ***$p<0.001$). Scale bars 100 µm (**A**) or 20 µm (**D**).

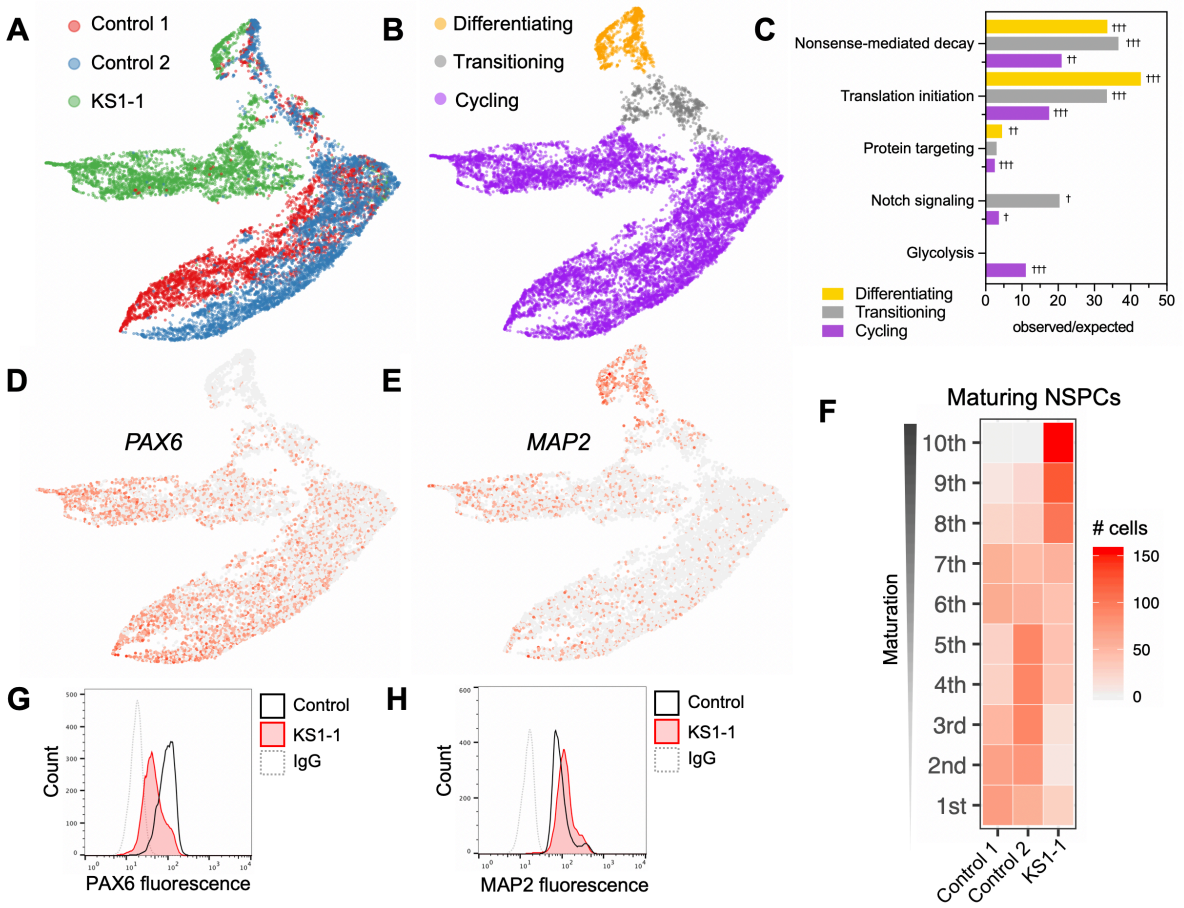

Figure 4. Transcriptional suppression of metabolic genes in cycling cells, and precocious neuronal differentiation in KS1 patient-derived NSPCs. (**A**) Single-cell RNA-seq profiling in patient and healthy control iPSC-derived NSPCs (~5,000 cells per patient), with Uniform Manifold Approximation Projection (UMAP) to visualize gene expression differences between cells. (**B**) NSPCs partitioned by maturation stage as defined by stage-specific marker expression, and (**C**) enriched gene networks, analyzed exclusively among DEGs for each NSPC subset (cycling, transitioning, and differentiating). (**D-E**) Representative UMAPs annotated by relative expression intensities of NSPC markers, revealing the maturation trajectory from early NSPCs (*PAX6*$^{+}$) to differentiating NSPCs (*MAP2*$^{+}$). (**F**) Heatmap comparing density of NSPCs along the maturation trajectory, defined by binned marker expression from earliest (1st) to most differentiated (10th) deciles, with KS1 cells disproportionately occupying the most mature bins. (**G-H**) Protein-level experimental validation of marker expression differences by flow cytometry in NSPCs from KS1 patient and controls, plotting fluorescence intensities of PAX6 and MAP2. Fisher's Exact Test (†FDR<0.05, ††FDR<0.01, †††FDR<0.001).

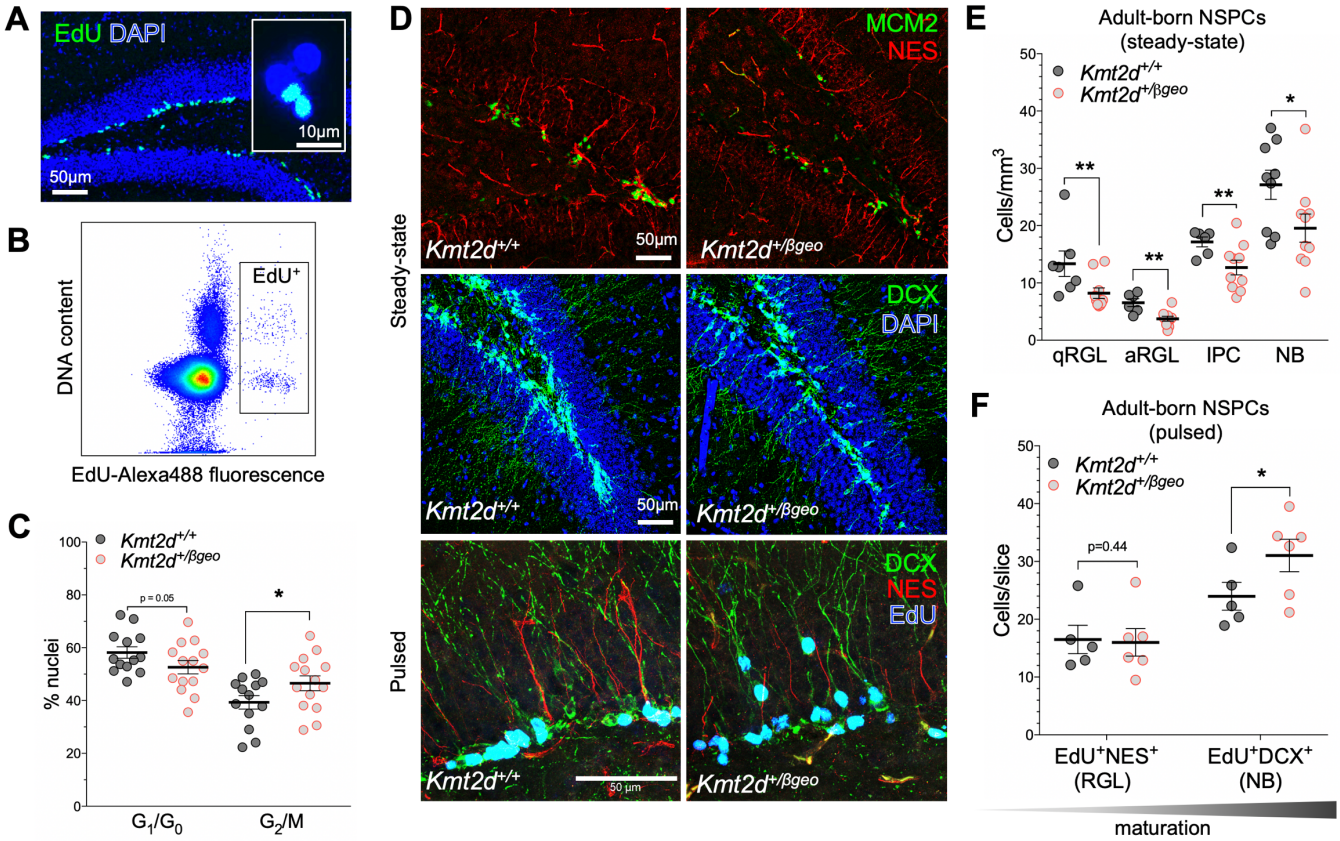

934
935
936 **Figure 5. In vivo defects of neurogenesis and NSPC differentiation in a *Kmt2d*$^{+/\beta geo}$ mouse model**
937 **of KS1**
938 (**A**) Immunostaining images of dividing (EdU-pulsed) dentate gyrus (DG) NSPCs, and nuclei purified
939 from micro-dissected DG by fluorescence-activated cell sorting (FACS) (**B**) of labeled nuclei. (**C**) Cell
940 cycle analysis in purified EdU$^+$ DG nuclei from *Kmt2d*$^{+/+}$ and *Kmt2d*$^{+/\beta geo}$ mice sampled 16 hours post-
941 pulse, using DAPI fluorescence (13-14 mice per genotype, 200-500 nuclei per mouse). (**D**)
942 Representative confocal immunostaining of neurogenesis markers in the DG of adult *Kmt2d*$^{+/+}$ and
943 *Kmt2d*$^{+/\beta geo}$ mice at steady-state (6-10 mice per genotype, 7-10 z-stack images per mouse) or after
944 EdU pulse (5-6 mice per genotype, 10 z-stack images per mouse). NES$^+$ radial glia-like (RGL) NSPCs,
945 in either quiescent (MCM2$^-$) or activated (MCM2$^+$) states (qRGL and aRGL, respectively), MCM2$^+$NES$^-$
946 intermediate progenitor cells (IPCs), and DCX$^+$ neuroblasts (NB) were quantified. (**E-F**) Quantification of
947 stage-specific NSPC densities (qRGL, aRGL, IPC, and NB) in adult *Kmt2d*$^{+/+}$ and *Kmt2d*$^{\beta/geo}$ mice at
948 steady-state (**E**) or after EdU pulse-chase (2 weeks) to birthdate differentiating NSPCs (**F**). Bars
949 indicate mean ± SEM. Student's t-test (*p<0.05, **p<0.01, ***p<0.001). Scale bars 50 µm, unless
950 specified (**A**, inset, 10 µm).
951

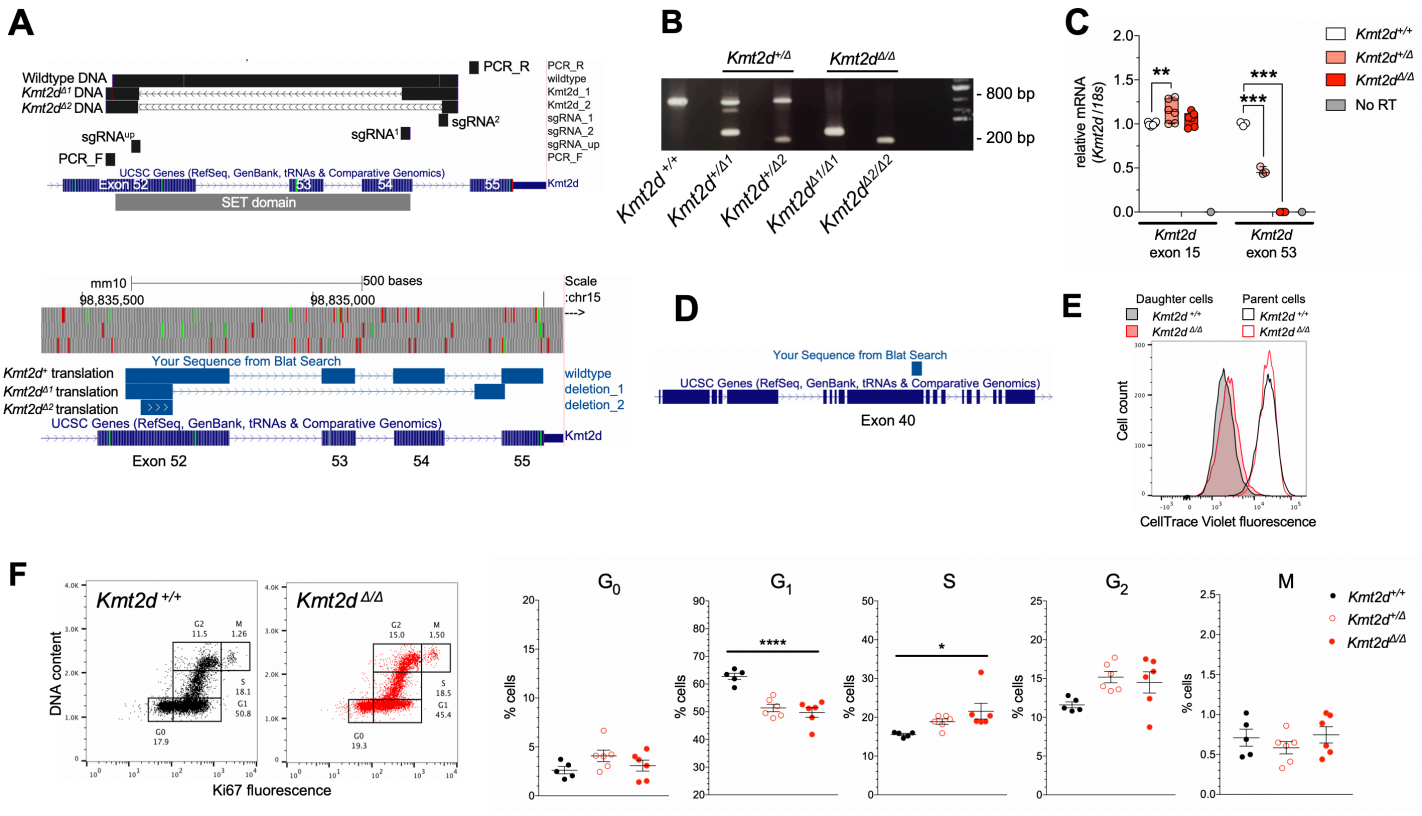

Supplementary Figure 1. CRISPR-targeted HT22 cells. (**A**) Sanger-sequenced DNA of wild-type (*Kmt2d*$^{+}$) and targeted (*Kmt2d*$^{\Delta}$) alleles in HT22 cells, mapped with sgRNAs and PCR primers, to *Kmt2d* locus (mm10) on chromosome 15. Mapping of Sanger-sequenced DNA after in silico translation to predict amino acid sequences illustrates premature termination codons (PTC) created in *Kmt2d*$^{\Delta 1}$ and *Kmt2d*$^{\Delta 2}$ alleles. (**B**) PCR with probes flanking sgRNA cut sites identifies experimental cell lines (*Kmt2d* $^{+/\Delta}$ and *Kmt2d*$^{\Delta/\Delta}$) compared to wild-type (*Kmt2d*$^{+/+}$). (**C**) RT-qPCR analysis of mRNA using probes spanning upstream exons (15-16) or exons within the deletion site (53-54). Two-way ANOVA with post hoc multiple comparisons. (**D**) Mapped peptide sequence of KMT2D antibody (Sigma). (**E**) Flow cytometric CellTrace fluorescence after 72 hours in HT22 cells. Increased intensity indicates less dye dilution, i.e. fewer cell divisions in mutants (left). Parental cell data confirm genotype-independent dye uptake (right) at 0 hours. (**F**) Cell cycle gating by flow cytometric analysis using Ki67 and DAPI to discriminate individual stages (G_0, G_1, S, G_2, M) in *Kmt2d*$^{+/+}$ and *Kmt2d*$^{\Delta/\Delta}$ cells, and quantification of each cycle phase. One-way ANOVA. Bars indicate mean ± SEM. Boxes indicate mean ± interquartile range; whiskers indicate minima and maxima. (*p<0.05, **p<0.01, ***p<0.001, ****p<0.0001).

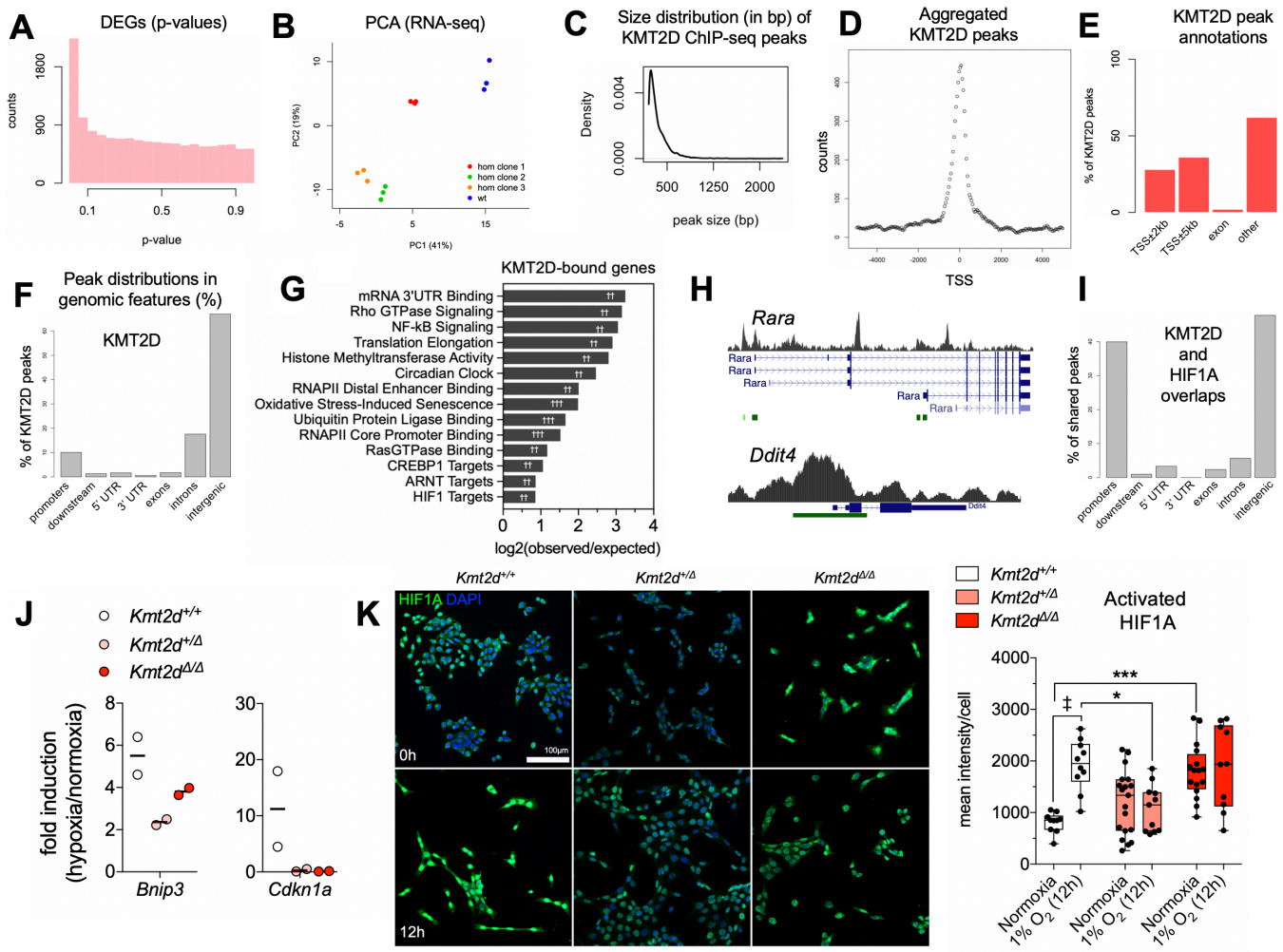

Supplementary Figure 2. HT22 cell RNA-seq and ChIP-seq analysis. (**A**) P-value distribution in *Kmt2d*$^{\Delta/\Delta}$ DEGs relative to wild-type indicates a well-calibrated test. (**B**) PCA visualizing clear expression differences in wild-type and *Kmt2d*$^{\Delta/\Delta}$ HT22 cells. (**C**) The size distribution (in bp) of KMT2D ChIP-seq peaks. (**D**) Validation of KMT2D peak distributions about gene TSSs and (**E-F**) genomic features. (**G**) Gene networks showing highest fold change in enrichment among genes proximal to KMT2D peaks (TSS±5 kb). Fisher's Exact Test (†FDR<0.05, ††FDR<0.01, †††FDR<0.001). (**H**) KMT2D peaks clustered at alternate TSSs of *Rara* gene and enhancer-like peaks at *Ddit4* gene. (**I**) Genomic features at overlapping KMT2D and HIF1A (26) ChIP-seq peaks. (**J**) RT-qPCR analysis of hypoxia-induced gene expression in HT22 cells, upon 1% O_2 exposure. One-way ANOVA (n.s.). (**K**) HIF1A nuclear fluorescence, i.e. activation, analysis. Representative z-stacked confocal images are shown with quantifications of nuclear HIF1A fluorescence. Two-way ANOVA with post hoc multiple comparisons (significance from wild-type, *p<0.05, **p<0.01, ***p<0.001; and from baseline, ‡p<0.01). Boxes indicate mean ± interquartile range; whiskers indicate minima and maxima. Scale bar 100 µm.

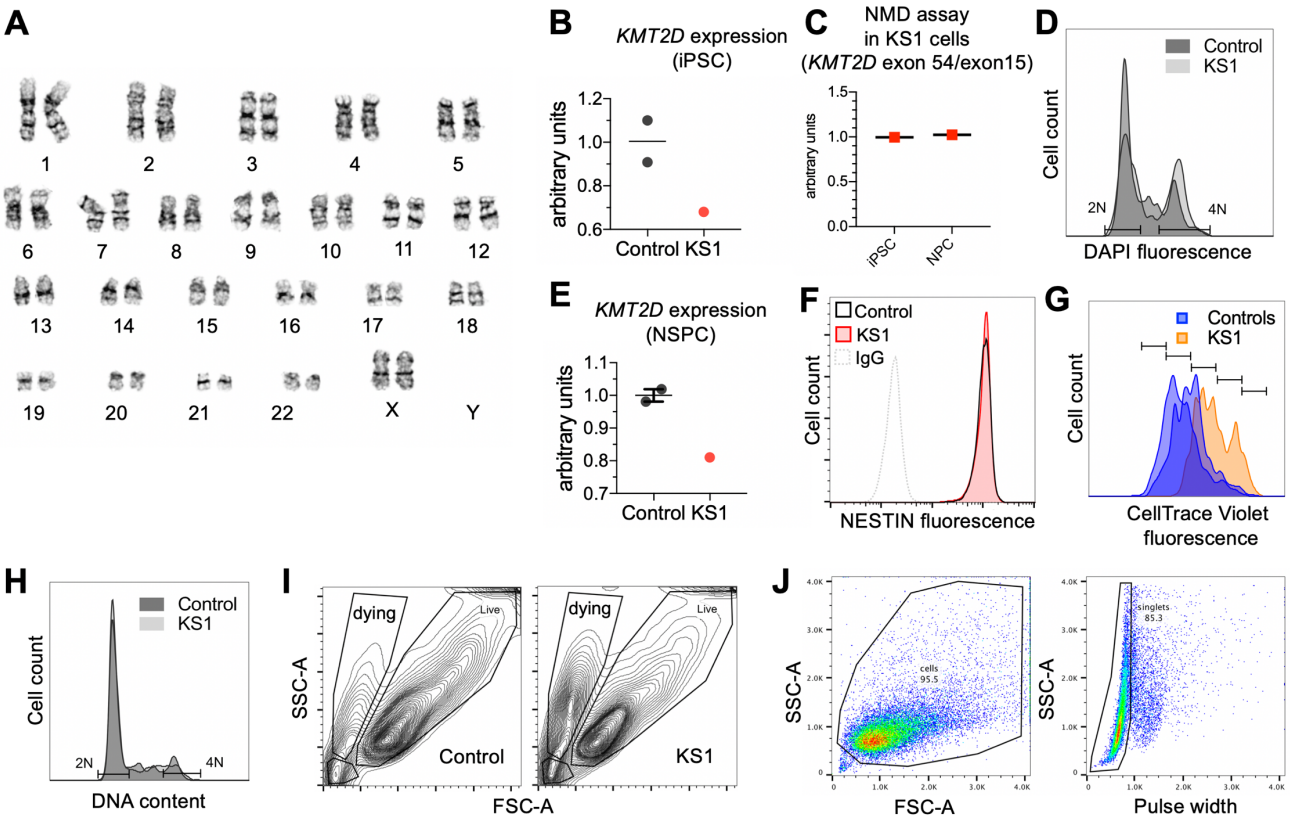

Supplementary Figure 3. iPSC and NSPC line validations and additional phenotyping. (**A**) 46, XX normal female karyotype in KS1-1 iPSCs. (**B**) RT-qPCR analysis of *KMT2D* (exon 15) expression in KS1 iPSCs compared to two healthy control iPSC lines (C1-2 and C3-1). Dots represent average of technical triplicates per patient line. Bars indicate mean. (**C**) RT-qPCR demonstrating equivalent exonic ratios of *KMT2D* exon 15 to exon 54, measured in technical triplicate, consistent with NMD of the entire transcript. (**D**) Flow cytometric analysis of DNA content by DAPI fluorescence in iPSCs. (**E**) RT-qPCR analysis of *KMT2D* (exon 15) expression in NSPCs derived from the KS1 and control iPSC lines, measured in technical triplicate. (**F**) Flow cytometric analysis of NES fluorescence intensity in KS1 and control NSPCs. (**G**) CellTrace Violet generational tracking showing fewer divisions (i.e. higher dye intensity) in patient-derived NSPCs over 72 hours. (**H**) Flow cytometric analysis of DNA content by DAPI fluorescence in NSPCs. (**I**) Sample flow cytometric gating for detection of scatter profiles indicative of cell death-associated cellular condensation. (**J**) Representative gating of viable cells and doublet discrimination in immunofluorescence-based flow cytometric analyses of iPSCs and NSPCs.

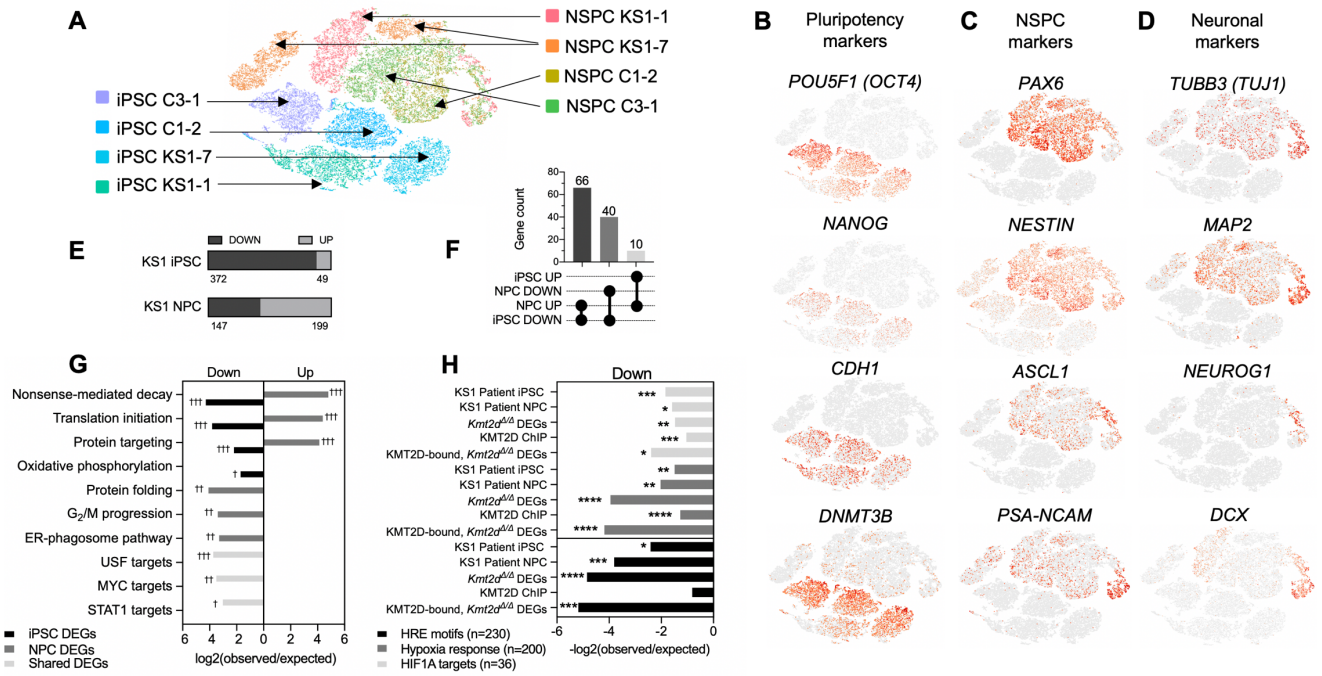

Supplementary Figure 4. iPSC and NSPC single-cell RNA-seq analysis. (**A**) t-stochastic neighbor embedding (tSNE) representation of iPSC and NSPC libraries sequenced on 10XGenomics platform. Cell clusters colored by cell type and patient ID. iPSCs and NSPCs derived from patient K1-7 were excluded from downstream analysis due to abnormal karyotype. (**B-D**) Representative tSNE of iPSC, NSPC, and neuronal markers demonstrating expected cell identities and revealing a gradient of cell maturation. (**E**) Proportions of DEGs down- or up-regulated in KS1 patient iPSCs or NSPCs compared to respective healthy controls, (**F**) DEG lists intersected for overlaps among down-regulated and up-regulated genes, and (**G**) Gene networks most enriched among differentially expressed genes (DEGs) in KS1 patient iPSCs and NSPCs relative to respective healthy controls, and DEGs shared in both cell types. (**H**) Significant enrichments of Hypoxia Response genes, HIF1A Direct Target genes, and genes containing the Hypoxia Response Element (HRE) RCGTG motif among observed DEGs in KS1 Patient iPSCs, KS1 Patient NSPCs, *Kmt2d*$^{\Delta/\Delta}$ HT22 cells, as well as KMT2D-bound genes in wild-type HT22 cells, and KMT2D-bound, down-regulated genes in *Kmt2d*$^{\Delta/\Delta}$ HT22 cells). Fisher's Exact Test (*p<0.05, **p<0.01, ***p<0.001; †FDR<0.05, ††FDR<0.01, †††FDR<0.001).

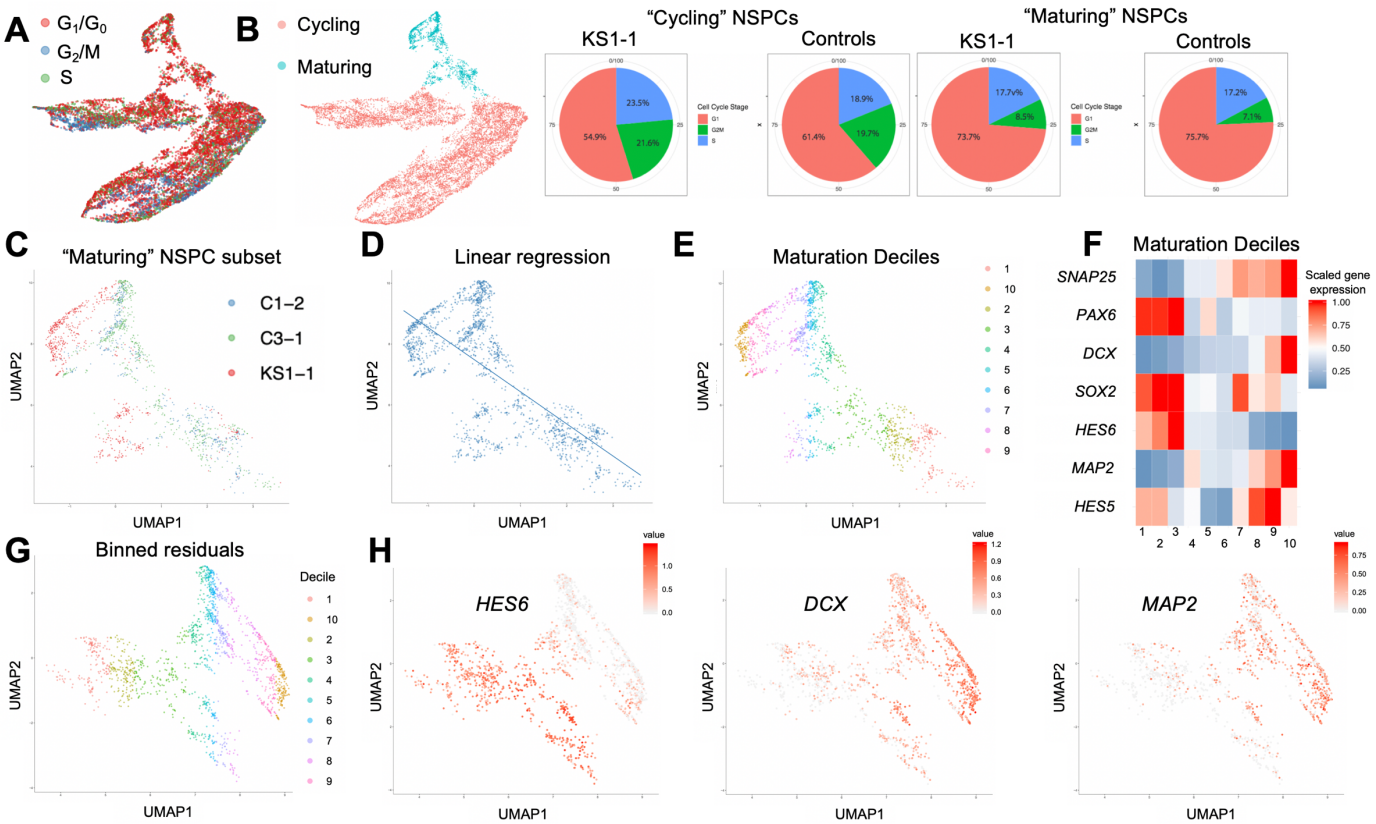

Supplementary Figure 5. Stratified scRNA-seq analysis of NSPCs. Uniform Manifold Approximation Projection (UMAP) of single-cell NSPC libraries partitioned by (**A**) cell cycle marker expression into subsets of G_1/G_0, S, and G_2/M cells, used for cycle phase-stratified differential expression analysis to rule out confounding differences in cell cycle phase composition on NSPC transcriptome comparisons. (**B**) Subset of "Cycling" versus non-cycling, "Maturing" NSPCs, which includes "Transitioning" and "Differentiating" cells as defined (**Figure 4B**), and UMAP-based cell cycle occupancies consistent with experimental FACS data (**Figure 3F**). (**C-H**) UMAP analysis of Differentiating NSPCs displaying (**C**) library patient ID's, (**D**) smooth linear regression fitted to define the maturation trajectory and (**E**) binned deciles of progressively maturing cells along the regression. (**F**) Relative expression of selected NSPC markers defining directionality of the maturation trajectory. (**G**) Binned residuals used to calculate deciles containing equal number of cells along the axis of differentiation. (**H**) Representative NSPC marker expression plotted over binned residuals.

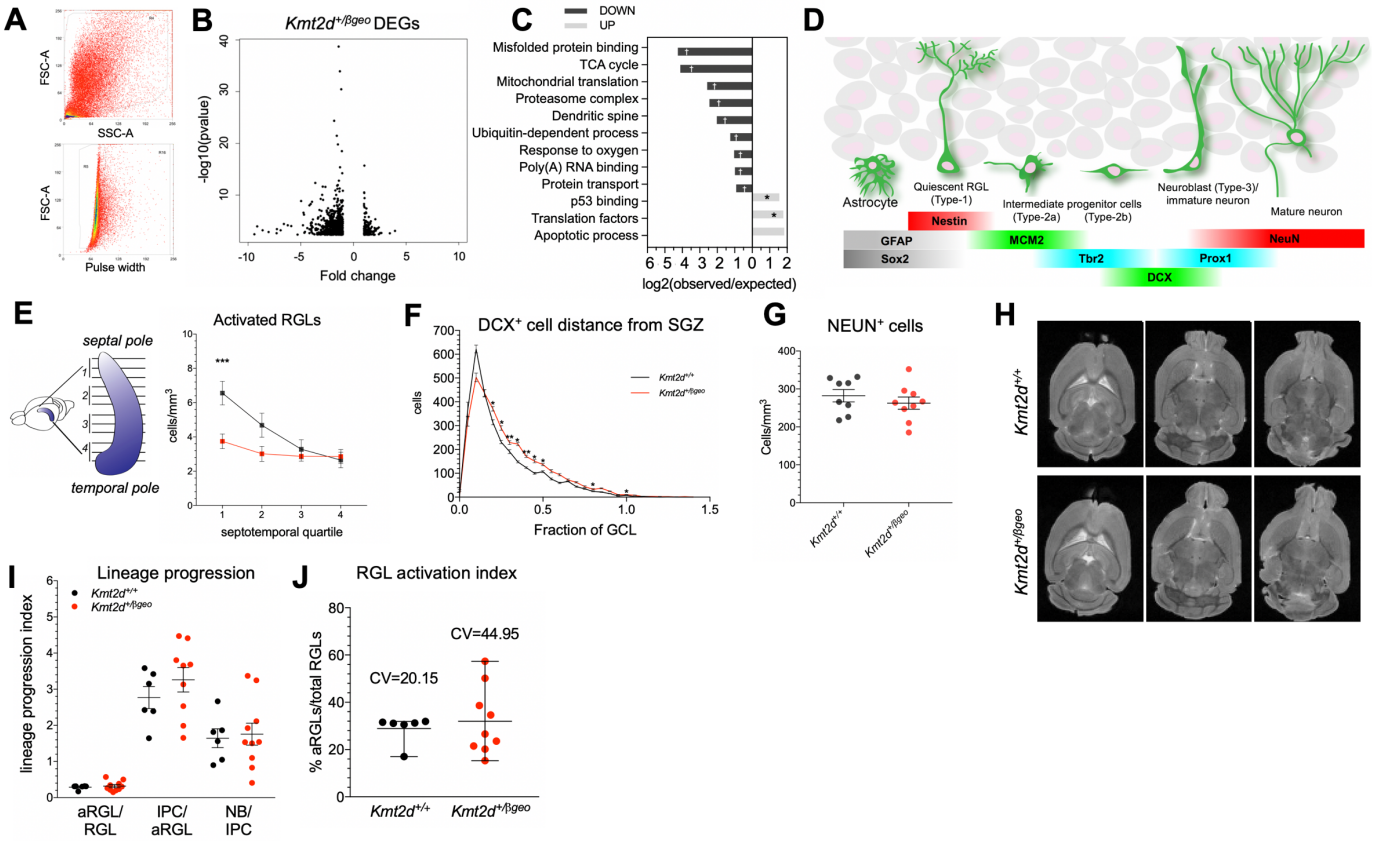

Supplementary Figure 6. Phenotyping of *Kmt2d*$^{+/\beta geo}$ mice. (**A**) Sample FACS gating for viable nuclei and doublet discrimination during purification of cycling EdU^{+} nuclei purified from *Kmt2d*$^{+/+}$ and *Kmt2d*$^{+/\beta geo}$ mice at 16 hours post-EdU pulse for RNA-seq and cell cycle analysis. (**B**) RNA-seq analysis of differential gene expression in purified EdU^{+} DG nuclei from *Kmt2d*$^{+/+}$ and *Kmt2d*$^{+/\beta geo}$ mice. (**C**) Gene networks most enriched among DEGs down- or up-regulated in *Kmt2d*$^{+/\beta geo}$ nuclei, showing transcriptional suppression of cellular metabolic pathways. Fisher's Exact Test (†FDR<0.05, ††FDR<0.01, †††FDR<0.001). (**D**) Schematic depicting marker expression during sequential stages of adult DG neurogenesis. (**E**) Serial ordering of perfusion-fixed brain slices enables anatomically-stratified analysis of neurogenesis, for quantification of activated RGL NSPC density along the septotemporal axis of the DG in *Kmt2d*$^{+/+}$ and *Kmt2d*$^{+/\beta geo}$ mice, indicating preferential disruption at the septal DG. Two-way ANOVA with post hoc multiple comparisons. (**F**) Quantification of DCX^{+} NB cell body distance from SGZ plane in 8-week-old mice (9-10 mice per genotype, >1,000 cells per mouse). Two-way ANOVA with post hoc multiple comparisons. (**G**) Quantification of RBFOX3/NEUN^{+} mature DG neurons in 8-week-old mice (8-9 mice per genotype, 10 z-stacks per mouse). Student's t-test (n.s.). (**H**) Sample images of T2-weighted MRI (9.4T) in PFA-fixed brains of female mice 4 months old. (**I**) Comparison of lineage progression index, an approximation of expansion potential for each cell type transition, indicates absence of genotype-associated blockages at any particular cell-type transition analyzed, and (**J**) increased Coefficient of Variance (CV) in RGL activation rates in *Kmt2d*$^{+/\beta geo}$ mice. Bars indicate mean ± SEM. (*p<0.05, **p<0.01, ***p<0.001).

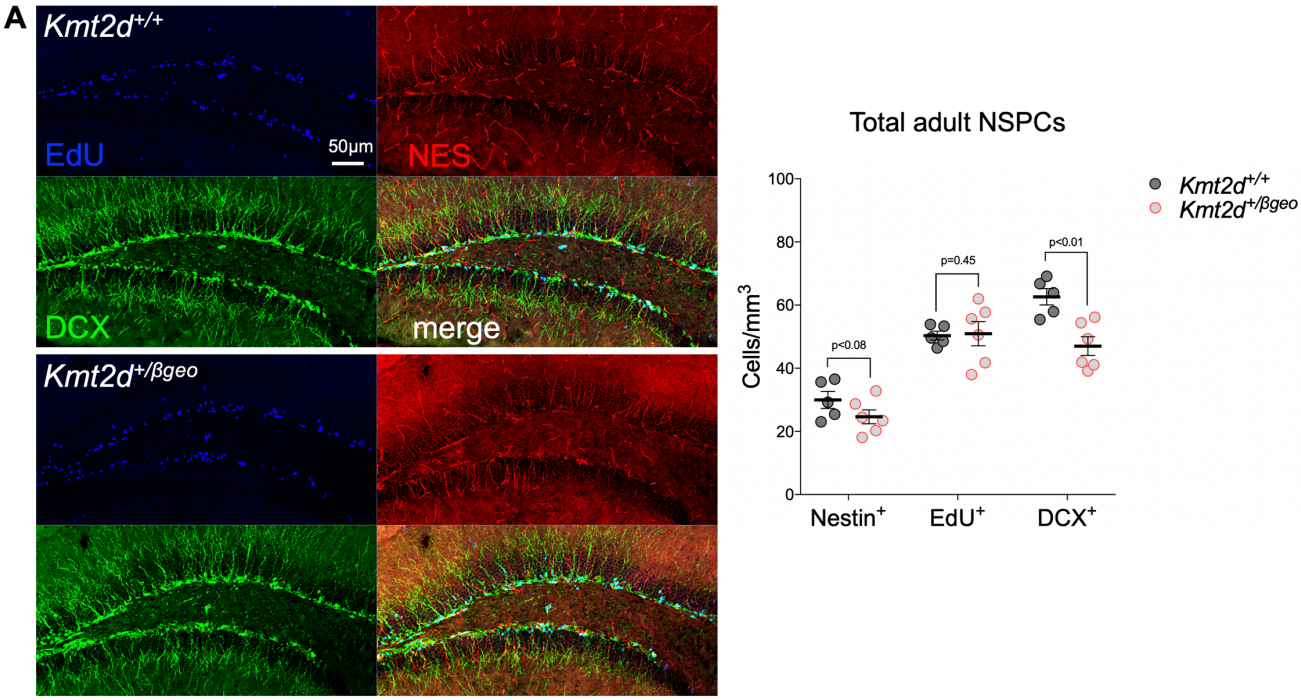

Supplementary Figure 7. Pulse-labeling to birth-date adult-born NSPCs in vivo. (**A**) Representative immunostaining from *Kmt2d*$^{+/+}$ and *Kmt2d*$^{+/\beta geo}$ mice (5-6 mice per genotype, 10 z-stacks per mouse) of EdU pulse-labeled cells extending a NES^{+} process (early RGL NSPCs) or DCX^{+} process (maturing NB NSPCs), showing the entire DG area quantified. Steady-state quantification of NSPCs and EdU-labeled NSPCs, confirming steady-state reduction of adult neurogenesis in *Kmt2d*$^{+/\beta geo}$ mice, despite their increased number of EdU^{+}DCX^{+} double-labeled NBs in the same experiment (**Figure 5E-F**). Bars indicate mean ± SEM, Student's t-test. Scale bar 50 µm.

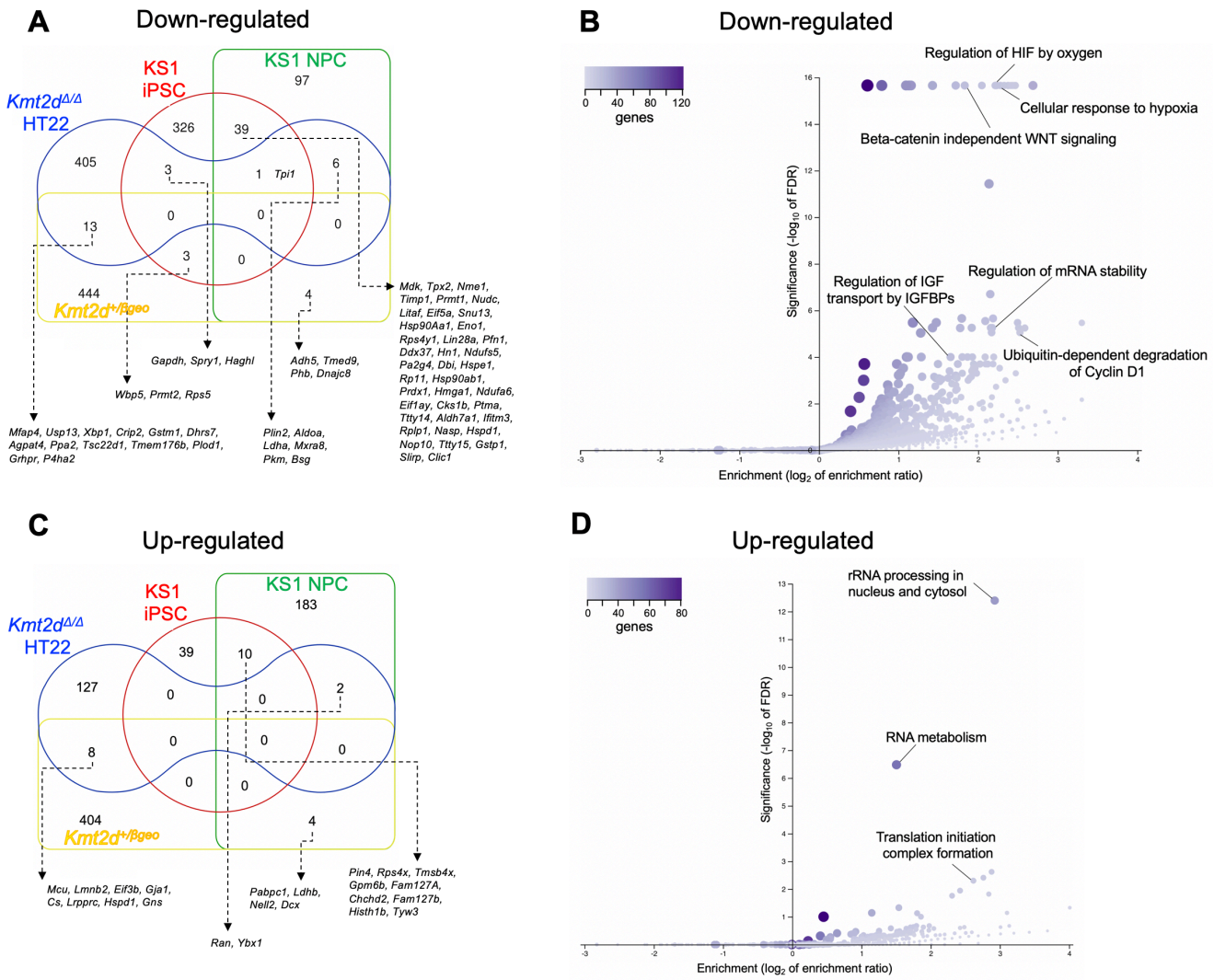

Supplementary Figure 8. Comparison of gene expression across KS1 models. (**A-B**) Euler diagram depicting shared transcriptional downregulation in KS1 models with individual genes (**A**) and pathways enriched among down-regulated genes from all KS1 models presently studied (**B**). (**C-D**) Euler diagram depicting transcriptional upregulation in KS1 models with individual genes (**C**) and pathways enriched among up-regulated genes from all KS1 models presently studied (**D**). Enrichments expressed as $\log_2$ of enrichment ratio. Significance expressed as $-\log_{10}$ of FDR. (WebGestalt).

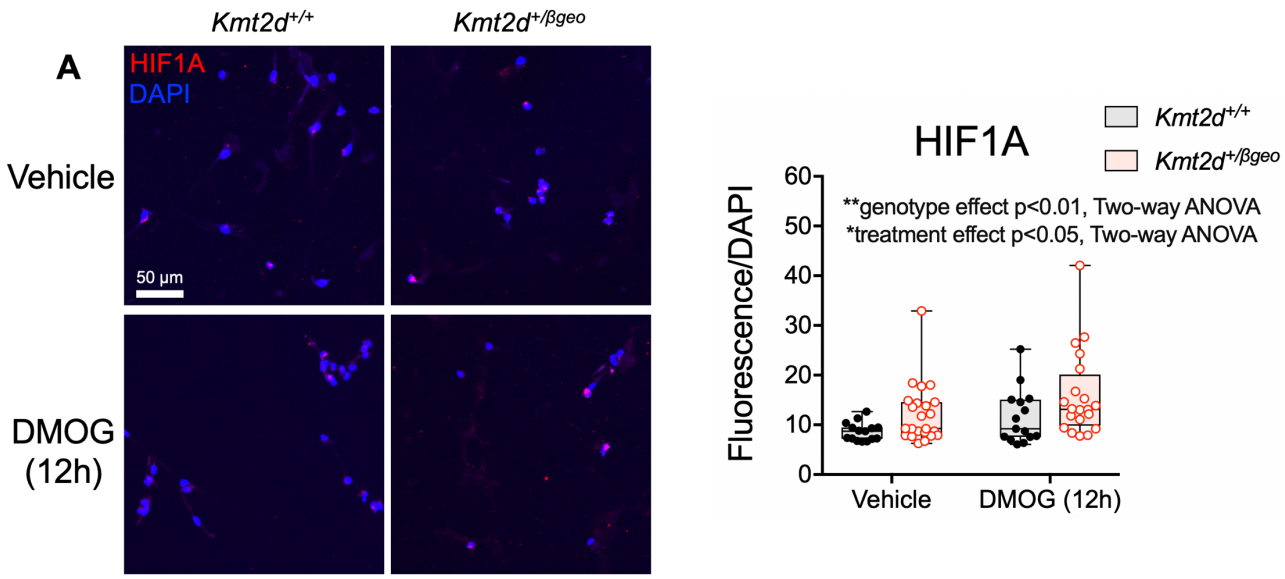

Supplementary Figure 9. HIF1A activation in primary hippocampal NSPCs. (**A**) Representative confocal images of primary hippocampal NSPCs isolated from micro-dissected DG of *Kmt2d*$^{+/+}$ and *Kmt2d*$^{+/\beta geo}$ mice, with quantification for analysis of HIF1A fluorescence inside the nucleus (DAPI^{+} volume). Two-way ANOVA with post-hoc multiple comparisons. (*p<0.05, **p<0.01, ***p<0.001). Boxes indicate mean ± interquartile range; whiskers indicate minima and maxima. Scale bar 50 µm.

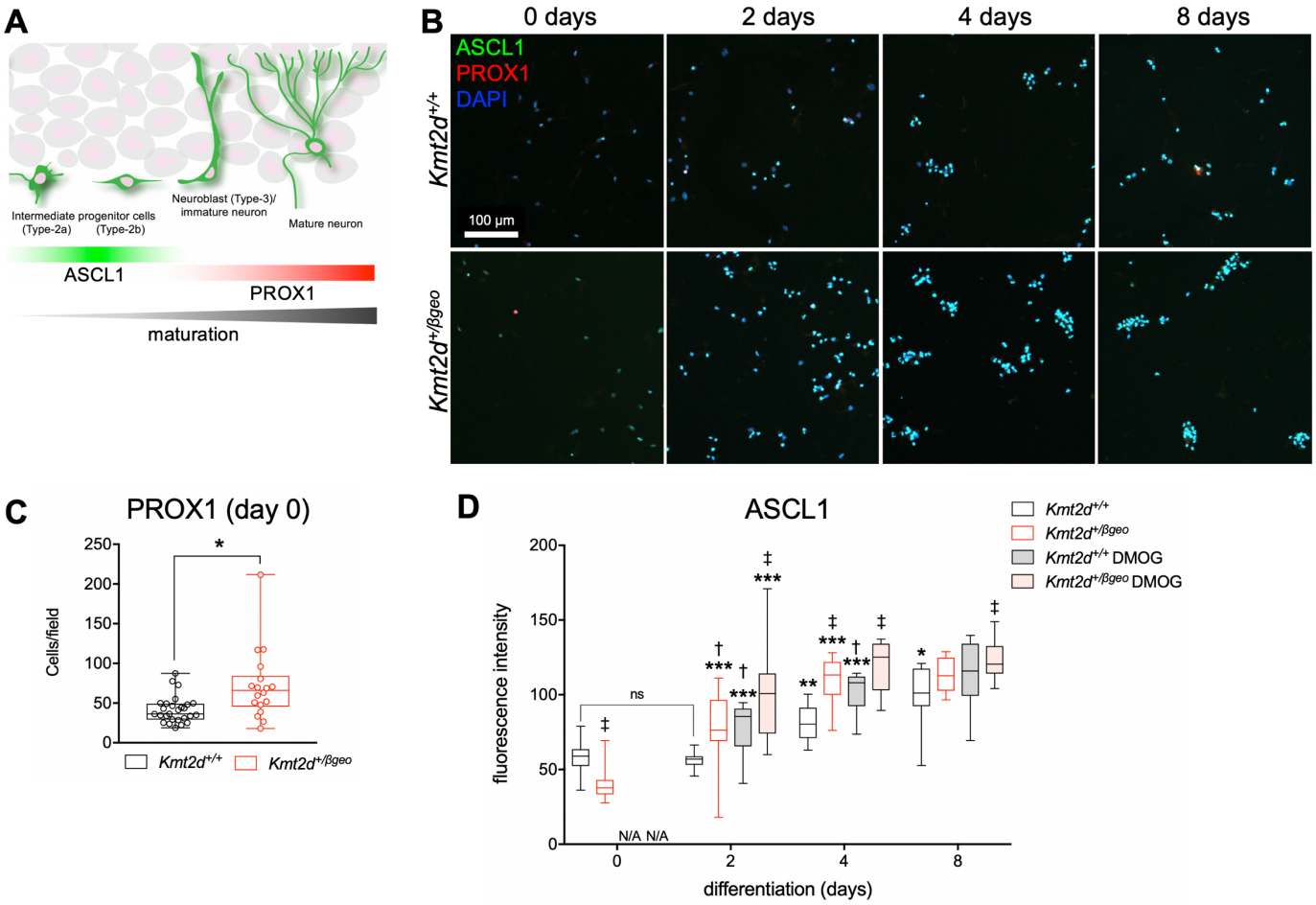

Supplementary Figure 10. Precocious in vitro differentiation of primary hippocampal NSPCs. (**A**) Schematic depicting developmental expression of pro-neural transcription factor ASCL1 and maturing neuronal marker PROX1 in adult-born DG neurons. (**B**) Representative confocal images for analysis of NSPCs differentiating between 0 and 8 days in primary hippocampal NSPCs isolated from micro-dissected DG of *Kmt2d*$^{+/+}$ and *Kmt2d*$^{+/\beta geo}$ mice, with quantifications (**C-D**). 22,307 cells analyzed individually across 176 fields of view. Two-way ANOVA with post hoc multiple comparisons. Boxes indicate mean ± interquartile range; whiskers indicate minima and maxima. (significance from previous time point *p<0.05, **p<0.01; ***p<0.001; significance from vehicle-treated wild-type †p<0.05, ‡p<0.01). Scale bar 100 µm.